

1 **Controls on the formation of porphyry Mo deposits: Insights from porphyry**
2 **(-skarn) Mo deposits in northeastern China**

3

4 Revision #2

5

6 Word Count: 9140

7

8 Hegen Ouyang^{1*}, John Caulfield², Jingwen Mao^{1,3}, Ruizhong Hu^{4,5}

9

10 ¹ MNR Key Laboratory of Metallogeny and Mineral Assessment, Institute of Mineral
11 Resources, Chinese Academy of Geological Sciences, Beijing, 100037, China

12 ² Central Analytical Research Facility, Queensland University of Technology, Brisbane,
13 4000, QLD, Australia

14 ³ China University of Geosciences, Beijing 100083, China

15 ⁴ State Key Laboratory of Ore Deposit Geochemistry, Institute of Geochemistry,
16 Chinese Academy of Sciences, Guiyang, 550081, China

17 ⁵ College of Earth and Planetary Sciences, University of Chinese Academy of Sciences,
18 Beijing, 100049, China

19

20 *Corresponding author. E-mail: oyhg1984@163.com

21

22

23

24

25

26

27

28

29

30

Abstract

31 Porphyry Mo deposits have traditionally been classified into two major classes; arc-
32 related and Climax-type based on the tectonic setting and chemistry of associated
33 intrusions. Although there is a consensus that porphyry Mo systems were formed by
34 the optimal coincidence of geological processes operating at different scales, it is
35 unclear what key parameter(s) render systems productive and whether the two
36 classes of porphyry Mo deposits are unique in their mode of formation, or if they
37 share fundamentally similar geological processes. These questions are important as a
38 clearer understanding of the optimum conditions for the formation of porphyry Mo
39 deposits is a prerequisite for more efficient exploration.

40 This contribution presents a detailed assessment of the factors affecting the
41 formation of porphyry Mo deposits through the investigation of barren and
42 mineralized intrusions from the arc-related Songbei-Yangjiazhangzi-Lanjiagou ore
43 zone and the Climax-type Hashitu deposit of northeastern China. Our results show
44 that the syn-mineralization intrusions from the Songbei-Yangjiazhangzi-Lanjiagou ore
45 zone are quite evolved ($\text{SiO}_2 \sim 75 \text{ wt\%}$; $\text{Na}_2\text{O}+\text{K}_2\text{O} \sim 8.7 \text{ wt\%}$) and are characterized
46 by apparent light rare earth element (LREE) enrichments ($\text{La}_N/\text{Yb}_N=2.7-33.1$) and
47 moderate negative Eu anomalies ($\text{Eu}/\text{Eu}^*=0.4-0.7$). They show enriched zircon Hf
48 isotopic compositions ($\epsilon_{\text{Hf}}(t)=-11.9 - -4.8$), indicating their parental magmas were
49 likely derived from an ancient crustal source. Melt inclusions from the Songbei-
50 Yangjiazhangzi-Lanjiagou syn-mineralization intrusions contain negligible F and Cl. In
51 contrast, Hashitu syn-mineralization intrusions are characterized by weak LREE
52 enrichments ($\text{La}_N/\text{Yb}_N=2.2-6.9$) and strong negative Eu anomalies ($\text{Eu}/\text{Eu}^*=0.02-$
53 0.10), with SiO_2 and $\text{Na}_2\text{O}+\text{K}_2\text{O}$ contents similar to the Songbei-Yangjiazhangzi-
54 Lanjiagou syn-mineralization intrusions. They show depleted zircon Hf isotopic
55 compositions ($\epsilon_{\text{Hf}}(t)=3.1-5.0$), indicating their parental magmas were likely derived
56 from a juvenile crustal source. Melt inclusions from the Hashitu syn-mineralization
57 intrusions contain up to 0.4 wt% F and 0.03 to 0.09 wt% Cl. However, in both cases,
58 the syn-mineralization intrusions are Mo-poor (1-7 ppm Mo), oxidized (above the

59 quartz-fayalite-magnetite buffer), water-saturated (4.4-7.8 wt% H₂O) and were
60 emplaced at palaeodepths of 3.3 to 8.3 km. These data imply that magma source
61 composition is not a key factor in the formation of porphyry Mo deposits. In
62 contrast, magma oxygen fugacity, water content and emplacement depth appear to
63 play fundamental roles in the formation of porphyry Mo deposits of both arc-related
64 and Climax-type.

65 Within individual deposits, no systematic differences between pre- and syn-
66 mineralization intrusions are observed in terms of magma source, fractionation
67 degree, oxygen fugacity, emplacement depth, and volatile and Mo contents. Instead,
68 a crucial apparent difference lies in the geometry of the intrusions, i.e., pre-
69 mineralization intrusions generally occur as flat, ponded bodies, whereas syn-
70 mineralization intrusions commonly develop as small stocks or dikes. Our results, in
71 combination with an examination of other porphyry Mo systems, suggest that the
72 sudden depressurization of magma chambers and subsequent venting of voluminous
73 fluids along focusing structures (such as small stocks or dikes) most likely plays a
74 critical role in the formation of porphyry Mo deposits of both arc-related and Climax-
75 type. The findings of this study indicate that fluid processes in the shallow crust are
76 pivotal for the formation of porphyry Mo deposits and that settings with ideal
77 magmatic-hydrothermal architectures are most likely to develop into productive
78 porphyry Mo systems.

79

80 **Keywords:** northeastern China, melt inclusions, focused fluid flow, arc-related
81 porphyry Mo deposit, Climax-type porphyry Mo deposit

82

83

84

85

86

87

88

Introduction

89 Porphyry Mo deposits, together with porphyry Cu-Mo deposits, represent the most
90 important sources of molybdenum worldwide. They were traditionally classified into
91 two major classes based on the tectonic setting and geochemistry of associated
92 intrusions: (1) Climax-type porphyry Mo deposits associated with fluorine-rich
93 (commonly >1.0 wt% F), highly evolved intrusions in extensional back-arc, post-
94 subduction or post-collisional settings ([Carten et al. 1993](#); [Ludington and Plumlee
2009](#)), and (2) arc-related porphyry Mo deposits associated with fluorine-poor (<0.1
95 wt% F), differentiated calc-alkaline granitoids in compressional arc-continent
96 subduction and collisional or continent-continent collisional settings ([Carten et al.
1993](#); [Taylor et al. 2012](#)). These two classes are considered the product of distinct
97 tectonic settings, which reflect fundamental differences in magma composition and
98 thermal regimes between extension and compression environments ([Carten et al.
1993](#); [Ludington and Plumlee 2009](#); [Taylor et al. 2012](#)). However, it is still unclear as
99 to whether the two classes of porphyry Mo deposits are unique in their model of ore
100 formation, or if they are formed by fundamentally similar geological processes at
101 upper crustal levels (e.g., [Stein and Hannah 1985](#); [Carten et al. 1993](#); [Audétat 2010](#),
102 [2015](#); [Xie et al. 2017](#); [Shu et al. 2019](#)). This is an important question to answer,
103 because if they are formed in the different ways, predicting the occurrence of
104 porphyry Mo deposits may be difficult. Conversely, if common processes in the
105 upper crust can alone account for the formation of porphyry Mo deposits of both
106 arc-related and Climax-type, then any setting with suitable magmatic-hydrothermal
107 architectures that provide optimum conditions for metal deposits could become
108 targets for exploration.

112 Over the past two decades, over sixty porphyry (-skarn) Mo deposits and
113 occurrences have been found in northeastern (NE) China ([Ouyang et al. 2013, 2020](#),
114 [2021](#); [Chen et al. 2017](#); [Shu et al. 2016, 2021](#)), making NE China the largest Mo ore
115 region on earth (total Mo resource >12.0 Mt; [Shu et al. 2021](#)). The deposits and
116 occurrences in NE China differ in terms of their tectonic settings, from compressional

117 arc-continent subduction and continent-continent collision, to extensional post-
118 subduction, and are all recognizable members of the established porphyry Mo
119 deposits family (Ouyang et al. 2013; Shu et al. 2016; Chen et al. 2017). These
120 features make NE China an ideal location in which to investigate the above-outlined
121 questions regarding the formation of porphyry Mo deposits.

122 In this contribution, one Climax-type porphyry Mo deposit (i.e., Hashitu; Fig. 1a)
123 and three arc-related porphyry-skarn Mo deposits (i.e., Songbei, Yangjiazhangzi and
124 Lanjiagou; Fig. 1a-b) from NE China were selected for study. We present major and
125 trace element, zircon Hf isotope, and silicate melt inclusion data (providing
126 information about the magmatic volatile and metal budget) for barren and
127 mineralized intrusions of the four deposits. A subset of the data used in this paper
128 has already been published in Ouyang et al. (2020), but the interpretations
129 presented here are new. In combination with our field observations, we aim to (1)
130 examine the importance of source protolith, magmatic processes and intensive
131 variables (e.g., magma volatile content, oxygen fugacity, and emplacement depth) in
132 producing porphyry Mo deposits, (2) discuss the results of the present study in
133 comparison with the published works on porphyry Mo deposits worldwide and (3)
134 provide a robust body of evidence to better understand the key factors affecting the
135 formation of porphyry Mo deposits of both arc-related and Climax-type.

136 **Geological background**

137 **Geology of the Songbei-Yangjiazhangzi-Lanjiagou ore zone**

138 The Songbei-Yangjiazhangzi-Lanjiagou ore zone is located in the eastern part of the
139 North China Craton (NCC; Fig. 1a), an Archean craton that was extensively thinned
140 during the late Mesozoic by delamination of the lithospheric mantle (Xu et al. 2006).
141 It consists of three large (≥ 0.1 Mt; Chen et al. 2017) porphyry (-skarn) Mo deposits;
142 Songbei, Yangjiazhangzi and Lanjiagou. The three Mo deposits are all associated with
143 an Early Jurassic composite intrusive complex, the Yangjiazhangzi pluton (Fig. 1b;
144 Ouyang et al., 2020). The bulk of the Yangjiazhangzi pluton comprises coarse-grained

145 syenogranite, which varies from equigranular to porphyritic, with an outcrop area of
146 approx. 200 km² (Fig. 1b), and was intruded by the fine-grained syenogranite and
147 granite porphyry intrusions (Huang et al. 1994; Wu et al. 2006). A number of
148 previous studies proposed that the Early Jurassic magmatism at Songbei-
149 Yangjiazhang-Lanjiagou formed in a continent-continent collisional setting related to
150 collision between the NCC and the amalgamated terranes of the Central Asian
151 Orogenic Belt (CAOB; e.g., Xiao et al. 2003; Zhang et al. 2014). However, an active
152 continental margin related to the subduction of the Paleo-Pacific plate has also been
153 proposed by other workers (e.g., Chen et al. 2007; Ge et al. 2007; Han et al. 2009;
154 Goldfarb et al., 2021). For these reasons, the porphyry (-skarn) deposits in the
155 Songbei-Yangjiazhangzi-Lanjiagou ore zone were classified as arc-related end
156 members of the established porphyry Mo deposit family (e.g., Zeng et al. 2013;
157 Ouyang et al. 2013, 2020; Shu et al. 2016, 2021).

158 Songbei is a skarn Mo deposit and contains an indicated resource of 0.17 Mt Mo
159 at an average grade of 0.10 wt% (Zeng et al. 2013). Intrusive rocks throughout the
160 mining area comprise pre-mineralization fine-grained syenogranite, syn-
161 mineralization granite porphyry and post-mineralization diabase (Fig. 1c; Zeng et al.
162 2013; Chu et al. 2017; Ouyang et al. 2020). The granite porphyry, exposed as dikes,
163 intruded along the contact zones between the Permian sandstone and Proterozoic to
164 Paleozoic limestone, or into the Proterozoic to Paleozoic limestone, within which
165 most of the Mo mineralization occurs. Molybdenum mineralization in the Songbei
166 deposit is represented by molybdenite-quartz±pyrite veinlets with sericite and
167 chlorite envelopes in the granite porphyry, or molybdenite-bearing skarn veins,
168 lenses and mantos in the limestone (Chu et al. 2017; Ouyang et al. 2020). Laser
169 ablation-inductively coupled plasma-mass spectrometer (LA-ICP-MS) zircon U-Pb
170 dating shows that the intrusion age of the granite porphyry is 184.0±2.0 Ma (1σ,
171 weighted mean ²⁰⁶Pb/²³⁸U age; Chu et al. 2017), in agreement with the isotope
172 dilution inductively-coupled plasma mass spectrometry (ID-ICP-MS) molybdenite Re-
173 Os weighted mean model age of 183.2±3.0 Ma (2σ) within uncertainty (Chu et al.
174 2017). In the present study, syn-mineralization rhyolite porphyry phase (previously

175 called granite porphyry) collected from the open pit (Fig. 1c) was chosen for further
176 study. The rhyolite porphyry (Fig. 2a) contains phenocrysts of quartz, pink alkali
177 feldspar and biotite, set in an aphanitic groundmass of similar mineralogy; accessory
178 minerals include apatite, titanite, zircon and magnetite.

179 The Yangjiazhangzi skarn Mo deposit is located ca. 3.0 km east of the Songbei
180 deposit (Fig. 1b). It contains 0.26 Mt Mo at an average grade of 0.14 wt% (Huang et
181 al. 1989). Intrusive rocks throughout the mining area comprise pre-mineralization
182 coarse-grained syenogranite and syn-mineralization fine-grained syenogranite (Fig.
183 1d; Ouyang et al. 2020). The coarse-grained syenogranite varies from equigranular to
184 slightly porphyritic and was intruded by the stock-like fine-grained syenogranite
185 (Huang et al. 1994). Zircon U-Pb dating of the coarse-grained syenogranite yielded a
186 weighted mean $^{206}\text{Pb}/^{238}\text{U}$ age of 186.1 ± 2.6 Ma (1σ , Cui 2019). The fine-grained
187 syenogranite intrusion is commonly equigranular in texture, but some parts are
188 porphyritic (Ishihara and Shibata 1980). Skarn Mo mineralization occurs mainly in
189 Precambrian carbonate rocks around the fine-grained syenogranite intrusion as
190 massive skarns and skarn veins with a minor proportion occurring as molybdenite-
191 quartz±pyrite veinlets hosted in the fine-grained syenogranite intrusion (Fig. 1d;
192 Huang et al. 1994). Zircon U-Pb dating of the fine-grained syenogranite returned a
193 weighted mean $^{206}\text{Pb}/^{238}\text{U}$ age of 183.7 ± 2.2 Ma (1σ , Cui 2019), in agreement with the
194 molybdenite Re-Os model ages of 187.0 ± 2.0 to 191.0 ± 6.0 Ma (2σ) within uncertainty
195 (Huang et al. 1994). Samples of the pre-mineralization granite porphyry (previously
196 called porphyritic syenogranite; Fig. 2b) and syn-mineralization granitic to rhyolitic
197 porphyry (Fig. 2c) were collected from outcrop and ore heap (dump) for the present
198 study. In hand specimen the pre-mineralization granite porphyry contains quartz,
199 pink alkali feldspar, plagioclase and biotite set in a fine-grained groundmass of
200 similar mineralogy. Accessory minerals include apatite, titanite, zircon and
201 magnetite. The main igneous minerals of the syn-mineralization granitic to rhyolitic
202 porphyry include quartz, pink alkali feldspar and biotite, with additional minor and
203 trace minerals including zircon, titanite and magnetite.

204 The Lanjiagou deposit is located ca. 20 km northwest of the Yangjiazhangzi
205 deposit (Fig. 1b), which has an indicated resource of 0.22 Mt Mo at an average grade
206 of 0.13 wt% (Huang et al. 1989). Mineralization at Lanjiagou is characterized by
207 molybdenite-bearing quartz veins, veinlets or breccias with sericite and chlorite
208 alterations hosted by a composite intrusive complex, comprising pre-mineralization
209 coarse-grained syenogranite and syn-mineralization fine-grained syenogranite (Fig.
210 1e; Ouyang et al., 2020). The pre-mineralization coarse-grained syenogranite
211 constitutes the bulk of the composite intrusion and was intruded by the stock-like
212 syn-mineralization fine-grained syenogranite. Zircon U-Pb dating of the fine-grained
213 syenogranite gave a weighted mean $^{206}\text{Pb}/^{238}\text{U}$ age of 185.0 ± 1.8 Ma (1σ , Zheng et al.
214 2014), which agrees within error with the molybdenite Re-Os weighted mean model
215 age of 183.1 ± 0.8 Ma (2σ , Han et al. 2009). Samples of the syn-mineralization fine-
216 grained syenogranite were chosen for further study. The syn-mineralization fine-
217 grained syenogranite (Fig. 2g) is equigranular and contains quartz, pink alkali feldspar
218 and biotite. Accessory minerals include zircon, magnetite, apatite and titanite.

219 **Geology of the Hashitu Mo deposit**

220 The Hashitu deposit is situated in the eastern part of the CAOB (Fig. 1a), a composite
221 accretionary orogen formed by the evolution of the Paleo-Asian ocean during the
222 Paleozoic to Triassic (Windley et al. 2007; Zhang et al., 2019; Liu et al., 2020), and by
223 the evolution of the Paleo-Pacific ocean and Mongolia-Okhotsk ocean during the
224 Early Jurassic to Cretaceous (Wu et al. 2005; Xu et al. 2013). The deposit contains an
225 indicated resource of 0.13 Mt Mo at an average grade of 0.13 wt% (Zhai et al. 2018).
226 Mineralization in the deposit is characterized by molybdenite-bearing quartz±fluorite
227 veins, veinlets or breccias with sericite and chlorite alteration in the pre-
228 mineralization monzogranite and syn-mineralization syenogranite (Fig. 1f; Appendix
229 Figure 1; Zhang et al. 2012; Zhai et al. 2014, 2018; Ouyang et al. 2020), which are the
230 two main lithologies cropping out in the deposit. The pre-mineralization
231 monzogranite varies from coarse equigranular to slightly porphyritic and is exposed

232 in the southern part of the deposit, where it covers an area of ca. 8 km² (Fig. 1f). It
233 has a zircon U-Pb weighted mean ²⁰⁶Pb/²³⁸U age of 147.0±1.0 Ma (1σ; Zhai et al.
234 2014). The stock-like syn-mineralization syenogranite intruded the monzogranite and
235 crops out mainly in the northern part of the deposit. Zircon U-Pb dating yielded a
236 weighted mean ²⁰⁶Pb/²³⁸U age of 143.0±2.0 Ma (1σ) for the syenogranite (Zhai et al.
237 2014). ID-ICP-MS molybdenite Re-Os dating yielded model ages varying from
238 150.0±2.0 to 144.0±2.0 Ma (2σ) and a weighted mean Re-Os model age of 147.0±1.0
239 Ma (2σ, n=9; Zhai et al. 2014). The magmatism and mineralization ages at Hashitu
240 are coeval with the timing of exhumation of metamorphic core complexes, extensive
241 mafic to felsic magmatism and development of intracontinental rift basins
242 throughout the eastern segment of the CAOB (Meng 2003; Wu et al. 2011). For this
243 reason, the Hashitu porphyry Mo deposit was classified as Climax-type end member
244 of the established porphyry Mo deposits family (e.g., Zhai et al. 2014; Chen et al.
245 2017; Ouyang et al. 2020; Shu et al. 2021). Diamond drilling at Hashitu has revealed
246 the presence of rhyolite porphyry and granite porphyry dikes at depth, which are
247 also genetically related to the ore-forming hydrothermal event (Appendix Figure 1;
248 Zhang et al. 2012; Ouyang et al. 2020). Samples of the pre-mineralization porphyritic
249 monzogranite and monzogranite, together with the syn-mineralization granite
250 porphyry and rhyolite porphyry, all collected from drill cores, were chosen for
251 further study. The main igneous minerals of the pre-mineralization porphyritic
252 monzogranite and monzogranite (Fig. 2h) include quartz, plagioclase, pink alkali
253 feldspar, and biotite, with additional minor and trace zircon, fluorite, titanite and
254 magnetite (Appendix Figure 2). The syn-mineralization granite porphyry and rhyolite
255 porphyry (Fig. 2i) are gray and consist of phenocrysts of quartz, alkali feldspar and
256 biotite set in fine-grained to aphanitic groundmass of the same mineralogy.
257 Accessory minerals include zircon, fluorite, magnetite, ilmenorutile, monazite,
258 xenotime and molybdenite (the latter occurring primarily as inclusions in quartz
259 phenocrysts; Appendix Figure 2; Ouyang et al. 2020).

260

Methods

261 **Whole-rock major and trace element analysis**

262 Whole-rock major and trace element compositions were analyzed at the Institute of
263 Crust Dynamics, China Earthquake Administration. For major element analysis,
264 powdered samples were fluxed with $\text{Li}_2\text{B}_4\text{O}_7$ at a mass ratio of 1:8 to produce
265 homogeneous glass disks at 1,250 °C using a V8C automatic fusion machine. The bulk
266 rock major elements were analyzed on fused glass discs using a Zetium sequential X-
267 ray fluorescence spectrometer. The value of loss on ignition (LOI) was determined at
268 a temperature of 1,000 °C. The accuracy and precision of the analytical results were
269 monitored using the GSR-3 and BHVO-2 standards. Analytical errors were better than
270 2 %.

271 Trace element analysis was conducted using solution inductively-coupled
272 plasma mass spectrometry (ICP-MS) on a Thermofisher X Series II. For the digestion
273 procedure, 25 mg of sample powder was precisely weighed and transferred into a
274 screw-top Teflon beaker. Powders were dissolved in a mixture of concentrated HF-
275 HNO_3 acids (1:5) at 170 °C for 72 hours. Once dissolved, solutions were evaporated
276 at 120 °C and twice redissolved using 1:1 HNO_3 . The final solutions were then diluted
277 1,000 times using 2 % distilled super-pure HNO_3 for ICP-MS analysis using In, Rh and
278 Re as internal standards. Standard solutions from American Lab Tech Company were
279 diluted to $1 \mu\text{g l}^{-1}$, $10 \mu\text{g l}^{-1}$, $50 \mu\text{g l}^{-1}$, and $100 \mu\text{g l}^{-1}$ to produce the calibration curves,
280 which showed linear regression coefficients ≥ 0.9999 . GSR-3 and BHVO-2 standards
281 were run as unknowns to evaluate the accuracy and precision of the analytical
282 results. Analytical errors for most elements were better than 2 %.

283 **Zircon Hf isotope analysis**

284 Zircon Hf isotope analysis was carried out using a Nu Plasma II MC-ICP-MS (Nu
285 Instruments) equipped with a 193 nm ArF excimer laser at the Nanjing FocuMS
286 Technology Co. Ltd, China. A circular 50 μm laser spot with a fluence of 6.0 J/cm^2 , a
287 repetition rate of 8 Hz and a duration of 40 s were selected for analysis. Helium was
288 used as the carrier gas to transport the ablated aerosol to the mass spectrometer.

289 Mass fractionation corrections for Hf and Yb isotopic ratios were based on
290 $^{176}\text{Lu}/^{175}\text{Lu}=0.02656$ (Blichert-Toft et al. 1997) and $^{176}\text{Yb}/^{173}\text{Yb}=0.7876$ (McCulloch et
291 al. 1977), respectively. To monitor the accuracy of this correction, every 5 sample
292 analyses were bracketed by analysis of reference zircons (91500, GJ-1, Mud Tank,
293 Penglai, and Plešovice). During analysis, the standard zircons gave $^{176}\text{Hf}/^{177}\text{Hf}$ ratios
294 consistent with recommended values (Sláma et al. 2008; Yuan et al. 2008), within
295 analytical error. A decay constant for ^{176}Lu of $1.867\times 10^{-11}\text{a}^{-1}$ was adopted (Söderlund
296 et al. 2004). Initial $^{176}\text{Hf}/^{177}\text{Hf}$ ratios, denoted as $\epsilon_{\text{Hf}}(t)$, were calculated relative to the
297 chondritic reservoir with a $^{176}\text{Hf}/^{177}\text{Hf}$ ratio of 0.282772 and $^{176}\text{Lu}/^{177}\text{Hf}$ of 0.0332
298 (Blichert-Toft and Albarède 1997). Single-stage Hf model ages (T_{DM}) were calculated
299 relative to the depleted mantle, which is assumed to have undergone linear isotopic
300 growth from $^{176}\text{Hf}/^{177}\text{Hf}=0.279718$ at 4.55 Ga to 0.283250 at the present day with a
301 $^{176}\text{Lu}/^{177}\text{Hf}$ ratio of 0.0384 (Griffin et al. 2000). Two-stage Hf model ages ($T_{2\text{DM}}$) were
302 calculated assuming a mean $^{176}\text{Lu}/^{177}\text{Hf}$ value of 0.015 for the average continental
303 crust (Griffin et al. 2002).

304 **Melt inclusion major and trace element analysis**

305 Melt inclusion major and trace element compositions were analyzed in non-
306 homogenized melt inclusions by LA-ICP-MS and in re-homogenized melt inclusions
307 by electron microprobe (EPMA) at the Bayerisches Geoinstitut, Germany. Detailed
308 analytical methods have been described previously by Audétat (2015) and Ouyang et
309 al. (2020).

310 For major and trace element analysis of non-homogenized melt inclusions,
311 selected inclusions from doubly-polished thin sections were analyzed with a 193 nm
312 ArF Excimer laser ablation system coupled to a PerkinElmer Elan DRC-e quadrupole
313 ICP-MS. The laser was operated at 5-10 Hz with an energy density of 3-10 J cm⁻². The
314 diameter of the laser beam was chosen such to ensure ablation of the entire melt
315 inclusion, whilst keeping the amount of ablated host mineral (i.e., quartz) to a
316 minimum. NIST SRM 610 was used as external standard and was analyzed twice at

317 the beginning and end of each block of up to 20 analyses. A well-characterized in-
318 house obsidian standard was analyzed in each session as an unknown to check
319 accuracy. Before each melt inclusion analysis, the quartz host was analyzed nearby
320 using a 40 μm circular spot to obtain a signal that could be used for Ti-in-quartz
321 (TitaniQ) thermobarometry (Huang and Audéat 2012). Internal standardization of
322 the melt inclusions was based on SiO_2 versus Al_2O_3 trends defined by corresponding
323 whole-rock data shown in Appendix Table S1. Uncertainties associated with the
324 analyses for most of the elements are estimated at 5 to 7 %.

325 To estimate the volatile contents (S, F, Cl and H_2O) of magmas, melt inclusions
326 in quartz phenocrysts were re-homogenized at conditions of 1.5 to 2.0 kbar and 780
327 $^\circ\text{C}$. The re-homogenized melt inclusions were then polished to the surface and
328 subsequently analyzed using a JEOL JXA-8200 microprobe equipped, using 15 kV, 20
329 nA and a beam defocused to 10 μm . Standardization was performed on albite (Na,
330 Si), orthoclase (K), spinel (Al), MnTiO_3 (Mn, Ti), metallic Fe, enstatite (Mg),
331 wollastonite (Ca), fluorite (F), vanadinite (Cl) and baryte (S). A topaz crystal
332 containing 20.5 ± 0.5 wt% F was measured as an unknown and returned expected F
333 values of 20.1 ± 0.2 wt%. Estimated H_2O contents of the re-homogenized melt
334 inclusions were obtained by taking the difference of the measured major element
335 analytical total to 100 wt% and taking into account O=F substitution (i.e., H_2O
336 contents equal 100 wt% minus the measured major element analytical total and O=F
337 substitution value; Devine et al. 1995). Due to alkali migration or Na loss during
338 EPMA analysis (e.g., Devine et al. 1995; Donovan and Vicenzi 2008), the estimated
339 H_2O contents are associated with an error of at least ± 1 wt%.

340 Results

341 Major and trace elements

342 Whole-rock major and trace element compositions for the pre- and syn-
343 mineralization intrusive samples from the arc-related Songbei-Yangjiazhangzi-
344 Lanjiagou ore zone and Climax-type Hashitu deposit are listed in Appendix Table S1

345 and shown in **Figure 3**. All the syn-mineralization intrusive samples are quite evolved
346 with SiO₂ contents between 71.79 and 77.06 wt% and total alkali content
347 (Na₂O+K₂O) of 6.74 to 9.19 wt% (**Fig. 3a**). On the SiO₂ versus K₂O diagram, they show
348 high-K calc-alkaline to shoshonite affinities (**Fig. 3b**). When plotted in primitive
349 mantle-normalized trace element diagrams (**Fig. 3c, 3e**), all samples display similar
350 patterns characterized by enrichments in Rb, Th, U and Pb, and depletions in Ba, Nb,
351 Sr and Eu. On the chondrite-normalized rare earth element (REE) diagrams (**Fig. 3d,**
352 **3f**), all samples are enriched in light rare earth elements (LREE) with respect to heavy
353 rare earth elements (HREE; La_N/Yb_N=2.7-33.1) and show little to moderate
354 fractionation between the middle REE (MREEs) and HREE (D_{Y_N}/Yb_N=0.4-1.3) with
355 apparent negative Eu anomalies (Eu^{*}=0.02-0.69).

356 Despite some compositional overlap, variations in the trace element
357 systematics of the syn-mineralization intrusions from the Hashitu deposit and
358 Songbei-Yangjiazhangzi-Lanjiagou ore zone can be discerned. The syn-mineralization
359 intrusions from the Hashitu deposit generally have low concentrations of Sr (11-52
360 ppm) and Ba (14-87 ppm), and high concentrations of Y (25-63 ppm; **Appendix Table**
361 **S1**). Their chondrite-normalized REE patterns are generally flat (La_N/Yb_N=3.2-6.9) and
362 exhibit strong negative Eu anomalies (Eu/Eu^{*}=0.02-0.10; **Fig. 3d**). In contrast, the
363 syn-mineralization intrusions from the Songbei-Yangjiazhangzi-Lanjiagou ore zone
364 are relatively enriched in Sr (60-179 ppm) and Ba (124-591 ppm), and depleted in Y
365 (7.8-29.0 ppm; **Appendix Table S1**). Their chondrite-normalized REE patterns show
366 apparent LREE enrichment (La_N/Yb_N=2.7-33.1) and moderately negative Eu
367 anomalies (Eu/Eu^{*}=0.4-0.7).

368 In addition, except for crosscutting relationships and petrographic differences
369 (**Figs. 1-2; Ouyang et al. 2020**), it is difficult to distinguish the pre- and syn-
370 mineralization intrusions in the individual deposits on the basis of their major and
371 trace element geochemistry (**Fig. 3**). This observation may reflect a common magma
372 source and similar extent of fractionation of the pre- and syn-mineralization
373 intrusions in the individual deposits investigated in the present study.

374 **Zircon Hf isotopes**

375 Zircon Hf isotopic compositions for the pre- and syn-mineralization intrusions from
376 the Songbei-Yangjiazhangzi-Lanjiagou ore zone and Hashitu deposit are reported in
377 [Appendix Table S2](#) and shown in [Figure 4](#). Zircons from the Yangjiazhangzi syn-
378 mineralization intrusion are characterized by enriched initial $^{176}\text{Hf}/^{177}\text{Hf}$ values that
379 vary between 0.282302 and 0.282456. Their corresponding initial $\epsilon_{\text{Hf}}(t)$ values are
380 restricted to -12.6 to -7.1 (-7.6 on average, $n=16$), which are similar to those of the
381 Yangjiazhangzi pre-mineralization intrusion of -12.1 to -7.5 (-9.2 on average, $n=14$).
382 The 19 analyzed zircons from the Lanjiagou syn-mineralization intrusion yield a range
383 of initial $\epsilon_{\text{Hf}}(t)$ values of -11.9 to -7.8 (-9.8 on average), which is comparable to the
384 pre- and syn-mineralization intrusions from the Yangjiazhangzi deposit. Zircons from
385 the Songbei syn-mineralization intrusion show relatively less enriched initial $\epsilon_{\text{Hf}}(t)$
386 values of -10.7 to -4.9 (-7.6 on average, $n=20$).

387 Initial $^{176}\text{Hf}/^{177}\text{Hf}$ values of the zircons from the Hashitu syn-mineralization vary
388 between 0.282772 and 0.282824 ([Appendix Table S2](#)). Corresponding initial $\epsilon_{\text{Hf}}(t)$
389 values ranging from 3.1 to 5.0 (4.1 on average, $n=19$). Zircons from the Hashitu pre-
390 mineralization intrusion yield initial $\epsilon_{\text{Hf}}(t)$ values ($\epsilon_{\text{Hf}}(t)=2.1-4.4$, 2.8 on average) similar
391 to those of the Hashitu syn-mineralization intrusion, but are in marked contrast to
392 the zircon initial $\epsilon_{\text{Hf}}(t)$ values of the pre- and syn-mineralization intrusions from the
393 Songbei-Yangjiazhangzi-Lanjiagou ore zone ([Fig. 4](#)).

394 **Melt inclusion compositions**

395 **The Songbei-Yangjiazhangzi-Lanjiagou ore zone**

396 LA-ICP-MS and EPMA data for melt inclusions from the Songbei-Yangjiazhangzi-
397 Lanjiagou ore zone and Hashitu deposit are provided in [Appendix Table S3](#) and
398 [Appendix Table S4](#). Melt inclusions from the Yangjiazhangzi pre-mineralization
399 intrusion are highly evolved ($\text{SiO}_2 \sim 80$ wt%), with 346 to 438 ppm Rb, 5 to 11 ppm Cs
400 and 4 to 6 ppm Mo ([Appendix Table S3](#)). No data on the volatile contents of the melt

401 inclusions from the Yangjiazhangzi pre-mineralization intrusion were obtained in this
402 study due to their relatively poorly preserved condition. Melt inclusions from the
403 Yangjiazhangzi syn-mineralization intrusion are finely crystallized to glassy (Fig. 2e,
404 2f). They are slightly less evolved than those of the pre-mineralization intrusion
405 (Rb=171-265 ppm; Cs=4-6 ppm), except one that contains 209 ppm Rb and 24 ppm
406 Cs. Molybdenum concentrations in the melt inclusions show a narrow range of 2 to 4
407 ppm. The melt inclusions contain ≤ 0.05 wt% Cl and variable H₂O (4.6 to 7.4 wt%),
408 whereas F contents were below the detection limit (0.15 wt%; Appendix Table S4).

409 Melt inclusions from the Lanjiagou syn-mineralization intrusion are finely
410 crystallized (Fig. 2j). They are comparable in composition with the melt inclusions
411 from the Yangjiazhangzi pre- and syn-mineralization intrusions, which are also highly
412 evolved (78-79 wt% SiO₂) with 222 to 341 ppm Rb, 2 to 8 ppm Cs and 4 to 5 ppm Mo.
413 No data on volatile contents were obtained for the melt inclusions from the
414 Lanjiagou syn-mineralization intrusion due to scarcity and the poorly preserved
415 nature of the inclusions.

416 Melt inclusions from the Songbei syn-mineralization intrusion are finely
417 crystallized (Fig. 2d). They are highly evolved (SiO₂~79 wt%) and typically contain
418 139 to 242 ppm Rb and 2 to 9 ppm Cs, except three that contain considerable Rb
419 (305-1269 ppm) and Cs (20-88 ppm). However, Mo concentrations in the melt
420 inclusions are relatively constant at 1 to 5 ppm. No volatile content data are
421 presented for the melt inclusions from the Songbei syn-mineralization intrusion
422 because the inclusions are partially decrepitated and thus were not considered for
423 re-homogenization.

424 **The Hashitu deposit**

425 Melt inclusions from the Hashitu pre-mineralization intrusion are coarsely
426 crystallized (Fig. 2k). They are rhyolitic in composition (SiO₂~80 wt%) with 301 to
427 646 ppm Rb and 5 to 48 ppm Cs (Appendix Table S3). Molybdenum concentrations in
428 the melt inclusions show a narrow rang of 1 to 5 ppm. Melt inclusions from the

429 Hashitu syn-mineralization intrusions are partly crystallized (Fig. 2i) and contain 198
430 to 731 ppm Rb, 8 to 53 ppm Cs and 1 to 7 ppm Mo, comparable with those from the
431 Hashitu pre-mineralization intrusion. They contain 4.4 to 7.8 wt% H₂O, ≤ 0.4 wt% F
432 and 0.03 to 0.09 wt% Cl (Appendix Table S4).

433 Discussion

434 Producing a porphyry Mo deposit clearly requires a series of favorable geological
435 conditions and processes including partial melting of the magma source regions in
436 the lower crust, the bulk composition of the magma, the metal and volatile content
437 of the magma, the oxidation state and crystallization conditions, and the
438 mechanisms of magma emplacement and volatile exsolution in the upper crust
439 (Richards 2011a and references therein). Moreover, there are two major classes of
440 porphyry Mo deposits (i.e., arc-related and Climax-type; Carten et al. 1993;
441 Ludington and Plumlee 2009; Taylor et al. 2012), which show contrasting tectonic
442 settings and geochemistry of associated intrusions. Such features raise an additional
443 set of petrogenetic and metallogenic questions relating to the formation of porphyry
444 Mo deposits. In the following sections, the various contributing factors mentioned
445 above are critically assessed based on the data presented in the present and former
446 studies.

447 Influence of magma source

448 As shown in Figure 4, zircon Hf isotopic compositions of the syn-mineralization
449 intrusions from the arc-related Songbei, Yangjiazhangzi and Lanjiagou deposits are
450 comparable, with most values centered around -12.0 to -8.0. These values indicate
451 that the parental magma of the syn-mineralization intrusions from the Songbei-
452 Yangjiazhangzi-Lanjiagou ore zone were most likely produced by partial melting of
453 ancient lower crust (Jiang et al. 2009), or through the interaction of enriched-mantle
454 derived melts with ancient crustal rocks and/or melts (Chen et al. 2007). By contrast,
455 the initial Hf isotopic compositions of the zircons from the Climax-type Hashitu syn-

456 mineralization intrusions are more radiogenic ($\epsilon_{\text{Hf}}(t)=3.1-5.0$; Fig. 4), implying that
457 their parental magmas were most likely produced by partial melting of juvenile lower
458 crust, probably initiated by upper mantle basaltic melts interacting with crustal rocks
459 and/or melts (Wu et al., 2002, 2003). Such contrasting zircon Hf isotopic
460 compositions of the syn-mineralization intrusions between the Songbei-
461 Yangjiazhangzi-Lanjiagou ore zone and the Hashitu deposit may relate to the two
462 fundamentally different orogenic systems from which the parental magmas
463 originated. The Songbei-Yangjiazhangzi-Lanjiagou ore zone is located in a reactivated
464 Archean craton (Fig. 1a). The lower crust beneath the craton mainly consists of
465 ancient crustal material (Xu et al. 2006). In contrast, the Hashitu deposit is situated in
466 the eastern part of the CAOB (Fig. 1a), which is a composite accretionary orogen
467 formed by the evolution of the Paleo-Asian, Paleo-Pacific and Mongolia-Okhotsk
468 oceans during the Phanerozoic (Wu et al. 2005; Windley et al. 2007; Xu et al. 2013).
469 The lower crust of the CAOB therefore comprises juvenile material, which generates
470 a distinct radiogenic hafnium signature when remelted (Wu et al., 2002, 2003;
471 Windley et al. 2007).

472 In fact, similar disparate isotope compositions of the syn-mineralization
473 intrusions were not only observed amongst arc-related and Climax-type porphyry
474 Mo deposits, but also in same class of porphyry Mo deposits. For example, previous
475 studies on the world-class Climax-type deposits (e.g., Henderson and Climax) in the
476 middle Rocky Mountains, western North America, showed that the parental magmas
477 of the causative intrusions in these deposits were derived from enriched lithospheric
478 mantle or ancient crust (Keith et al. 1993; Pettke et al. 2010), contrasting with the
479 syn-mineralization intrusions from the Climax-type Hashitu deposit. Neodymium
480 isotopic compositions of the syn-mineralization intrusions from the arc-related
481 Endako porphyry Mo deposit indicate that the parental magmas of the causative
482 intrusions in this deposit were mainly formed by partial melting of juvenile material
483 (Whalen et al. 2001), which is in marked contrast to the syn-mineralization intrusions
484 from the arc-related Songbei, Yangjiazhangzi and Lanjiagou deposits.

485 The above discussion indicates that unique magma sources may not be required
486 for the formation of porphyry (-skarn) Mo deposits of both arc-related and Climax-
487 type. This conclusion is further supported by the zircon Hf isotopic compositions of
488 the pre-mineralization intrusions from the Songbei-Yangjiazhangzi-Lanjiagou ore
489 zone and Hashitu deposit, which are comparable to those of the syn-mineralization
490 intrusions in the individual cases (Fig. 4). Consequently, in addition to the nature of
491 the magma source, other factors may be more critical for the formation of both arc-
492 related and Climax-type porphyry Mo deposits.

493 **Influence of the bulk composition of ore-forming magmas**

494 Whole-rock major and trace element data show that the geochemistry of associated
495 intrusions of the two classes of porphyry Mo deposits investigated in the present
496 study do exhibit certain characteristics that mark each class unique. The syn-
497 mineralization intrusions from the Climax Hashitu deposit are depleted in TiO₂ (0.07
498 wt% on average), Sr (11-52 ppm) and Ba (14-89 ppm), and enriched in Rb (280 ppm),
499 Nb (15 ppm) and Y (25-94 ppm). They generally exhibit flat chondrite-normalized REE
500 patterns with strong negative Eu anomalies (Fig. 3d), indicating extensive fractional
501 crystallization of a plagioclase rich assemblage (Whalen et al. 1987; Wu et al. 2017).
502 By contrast, the syn-mineralization intrusions from the arc-related porphyry (-skarn)
503 Mo deposits of Songbei, Yangjiazhangzi and Lanjiagou are relatively enriched in TiO₂
504 (0.16 wt% on average), Sr (42-179 ppm) and Ba (84-591 ppm), and depleted in Y (7.8-
505 29.0 ppm). Their chondrite-normalized REE patterns are characterized by apparent
506 LREE enrichment and moderate negative Eu anomalies (Fig. 3f), which most likely
507 reflects the predominance of plagioclase-amphibole in the fractionating mineral
508 assemblage or in the restite (Romick et al. 1992; Richards 2011b). The association of
509 Climax-type and arc-related porphyry (-skarn) Mo deposits with distinct bulk magma
510 compositions (as described above) could suggest some sort of petrogenetic control
511 on the formation of porphyry Mo deposits, which has been mainly ascribed to
512 differences in tectonic setting and thermal regime (e.g., Carten et al. 1993; Ludington

513 [and Plumlee 2009; Richards 2011a; Taylor et al. 2012](#)). However, compared to
514 intrusions associated with typical Climax-type and arc-related porphyry Mo deposits
515 ([Carten et al. 1993; Ludington and Plumlee 2009; Taylor et al. 2012](#)), the syn-
516 mineralization intrusions from the four deposits investigated here exhibit some
517 hybrid characteristics, with Hashitu more closely resembling the former, and
518 Songbei, Yangjiazhangzi and Lanjiagou the latter. This may suggest that intrusions
519 associated with a certain class of porphyry Mo deposit could show a relatively broad
520 compositional variation. This inference is consistent with the identified geochemical
521 features of the intrusions associated with arc-related porphyry Mo deposits, which
522 exhibit a wide variation in SiO₂ contents ranging from 65.0 to 77.0 wt% ([Taylor et al.](#)
523 [2012](#)).

524 The relatively broad compositional variation shown by intrusions associated
525 with a certain class of porphyry Mo deposit can be caused by a variety of
526 mechanisms, including heterogeneous protolith sources, anatectic style and degree
527 of fractional crystallization ([Richards, 2011a and references therein](#)), and the exact
528 nature for the specific cases investigated in the present study is beyond the scope of
529 this contribution. Meanwhile, it suggests that the bulk composition of ore-forming
530 magmas, which is in turn controlled by other factors, such as tectonic setting,
531 composition of source rocks, degree of partial melting and extent of fractionation, is
532 not a critical control on the formation of porphyry Mo deposits of both arc-related
533 and Climax-type. As shown in [Figure 3](#), the bulk compositions of the pre- and syn-
534 mineralization intrusions in the individual deposits of both arc-related and Climax-
535 type are overall similar, further implying other factors are more important for the
536 formation of porphyry Mo deposits.

537 **Molybdenum content of the ore-forming magma**

538 LA-ICP-MS data show that melt inclusions from the syn-mineralization intrusions of
539 the three arc-related Mo deposits in the Songbei-Yangjiazhangzi-Lanjiagou ore zone
540 are all poor in Mo (ranging from 1 to 5 ppm Mo with an average of 3 ppm), and

541 similar to those of the Climax-type Hashitu deposit of 1 to 7 ppm ([Appendix Table S3](#);
542 [Fig. 5b](#)). The Mo-poor composition of melt inclusions could result from molybdenite
543 saturation (e.g., [Audétat et al. 2011](#)), Mo partitions into Ti-bearing minerals ([Cerny et](#)
544 [al. 2005 and references therein](#)), or that Mo was transported into the fluid phase
545 prior to melt inclusion growth (e.g., [Audétat, 2010](#)). [Ouyang et al. \(2020\)](#) observed
546 magmatic molybdenite inclusions in quartz phenocrysts of the Hashitu syn-
547 mineralization intrusions ([Appendix Figure 2c](#)). As shown in [Figure 5a-b](#), the Mo
548 contents of the melt inclusions in this deposit generally increase with increasing
549 degree of melt fractionation. This may suggest that the magmatic molybdenite
550 inclusions in the Hashitu deposit are too sparse to account for the Mo-poor
551 composition of the analyzed melt inclusions. Moreover, in this study, non magmatic
552 molybdenite inclusions were observed in the syn-mineralization intrusions of the
553 Songbei-Yangjiazhangzi-Lanjiagou ore zone. These two observations generally
554 preclude a link between the Mo-poor composition of the analyzed melt inclusions
555 and molybdenite saturation. Under reduced conditions, wherein the dominant
556 speciation of Mo is Mo⁴⁺, Mo tends to partition into Ti-bearing minerals (e.g.,
557 ilmenite, titanite and biotite) resulting in Mo-poor magmas, as the ionic radius of
558 Mo⁴⁺ is nearly identical to Ti⁴⁺ ([Cerny et al. 2005 and references therein](#)). Our
559 petrographic observations show that magnetite and titanite are the common
560 accessory minerals in the syn-mineralization intrusions of the Songbei-
561 Yangjiazhangzi-Lanjiagou ore zone and Hashitu deposit, indicating the relatively
562 oxidized nature of the syn-mineralization intrusions in both cases (e.g., [Dilles 1987](#)).
563 It follows that the Mo-poor composition of the melt inclusions investigated in this
564 study cannot be solely ascribed to the partitioning of Mo into Ti-bearing minerals
565 prior to melt inclusion growth.

566 As shown in [Figure 5](#), the Mo contents of the melt inclusions in the individual
567 deposits investigated in this study generally increase with increasing degree of melt
568 fractionation, as indicated by increasing Rb and Cs concentrations. This feature
569 generally precludes the possibility that Mo partitioned into magmatic molybdenite,
570 Ti-bearing minerals or a fluid phase prior to the growth of melt inclusions. In fact, the

571 evolutionary trends of Rb, Cs and Mo (Fig. 5a-b) generally overlap with the trends
572 shown by known arc-related and Climax-type deposits (Fig. 5c-d). This indicates that
573 the melt from which the inclusions formed was in fact Mo poor, rather than
574 undergoing Mo loss prior to inclusion entrapment. The Mo contents of the syn-
575 mineralization inclusions of the two class of porphyry Mo deposits investigated in
576 this study (2.7 ppm on average; Appendix Table S3) are generally higher than the less
577 evolved ($\text{SiO}_2 < 70$ wt%) medium to high K calc-alkaline granitoids of 1 to 1.5 ppm
578 (Cerny et al. 2005 and references therein), but are consistent with the Mo
579 concentrations of mineralization granitoids (3 to 4 ppm) associated with both typical
580 arc-related and Climax-type deposits (Lowenstern et al. 1993; Audétat, 2015; Zhang
581 and Audétat 2017; Ouyang et al. 2021). These results indicate that high Mo
582 concentrations may not be necessary for the formation the porphyry Mo deposits of
583 both arc-related and Climax-type, although anomalously Mo rich sources will
584 undoubtedly increase the probability of mineralization. This conclusion is further
585 supported by two observations: (1) no systematic difference in Mo contents
586 between the pre- and syn-mineralization intrusions is evident within each deposit
587 investigated in this study (Fig. 5b), and (2) the melt inclusions investigated in this
588 study contain comparable Mo contents to those of barren intrusions (e.g., Zhang and
589 Audétat 2018).

590 **Effect of magma F and Cl contents**

591 EPMA analysis of the re-homogenized melt inclusions show that melt inclusions from
592 the Climax-type Hashitu syn-mineralization intrusions contain ≤ 0.4 wt% F, which is in
593 marked contrast to those of the syn-mineralization intrusions from the arc-related
594 Songbei-Yangjiazhangzi-Lanjiagou ore zone, with F contents below the EPMA
595 detection limit of 0.15 wt% (Fig. 6a). The relatively F-rich feature of the Hashitu syn-
596 mineralization intrusions is consistent with the occurrence of magmatic fluorite in
597 the intrusions (Appendix Figure 2a) and appreciable hydrothermal fluorite in the
598 deposit (Zhai et al. 2018). It also consistent with the observation that porphyry Mo

599 deposits formed in within-plate settings (Climax-type) generally contain more F than
600 their arc-related counterparts (e.g., [Carten et al. 1993](#); [Ludington and Plumlee 2009](#);
601 [Zhang and Audétat 2017](#)). However, compared to the two typical Climax-type
602 deposits of Climax and Urad-Henderson, which contain up to 3.9 wt% F ([Audétat,](#)
603 [2015](#); [Zhang and Audétat, 2017](#)), the Hashitu system is still F-poor.

604 Fluorine is known to extend magma fractionation by reducing minimum-melt
605 temperature and melt viscosity ([Dingwell et al. 1985](#)), and thus enhances Mo
606 concentration processes and mineralization potential ([Carten et al. 1993](#)). Indeed, as
607 shown in [Figure 5c-d](#), the most highly fractionated melts (10 times more fractionated
608 than the melts investigated in this study), which have distinctly higher Mo contents
609 (up to 100 ppm), are from the two highly F-enriched Climax-type deposits of Climax
610 (3.1-3.9 wt%; [Audétat 2015](#)) and Urad-Henderson (0.5-1.0 wt%; [Zhang and Audétat](#)
611 [2017](#)). Correspondingly, the Mo grades and metal endowments of these deposits are
612 generally higher than other F-poor systems ([Fig. 7a](#)). However, this trend is not so
613 apparent in the present and selected existing case studies. For example, compared
614 to melt inclusions from the relatively F-enriched Hashitu (≤ 0.4 wt% F; [this study](#)),
615 Pine Grove (0.2-0.9 wt% F; [Lowenstern 1994](#); [Zhang and Audétat 2017](#)) and Silver
616 Creek (0.25-0.32 wt% F; [Zhang and Audétat 2017](#)) systems, those from the F-poor
617 Songbei, Yangjiazhangzi and Lanjiagou systems (<0.15 wt% F; [this study](#)) are similar
618 evolved with comparable Mo contents and/or ore grades and reserves ([Figs. 5, 7](#)).
619 This implies that magma F content may not a prerequisite for the formation of
620 porphyry Mo deposits, although elevated F can indeed extend fractionation and thus
621 enhance the melt Mo concentration and ore grade or reserve.

622 As shown in [Figure 6a-b](#), there is a positive correction between magma F and Cl
623 contents. The high Cl content in F-rich magmas may be related to the fact that F can
624 increase the solubility of Cl in melts ([Webster 1997](#)). However, regardless of the Cl
625 content, all magmas studied here produced economic Mo mineralization. This
626 suggests that a high magma Cl content is also not a requisite to produce economic
627 porphyry Mo mineralization. This conclusion is permissively consistent with
628 experimental results that demonstrate that, in porphyry Mo systems, Mo is

629 dominantly transported as a hydroxyl complex and that high Cl concentrations may
630 inhibit the transport of Mo by destabilizing the hydroxyl complex (Keppler and
631 Wyllie, 1991).

632 **Influence of magma emplacement depth**

633 In this study, titanium-in-quartz (TitaniQ) thermobarometry of Huang and Audétat
634 (2012) was used to estimate the crystallization pressures (i.e., magma emplacement
635 depths) at which the magmas were emplaced, based on melt inclusion LA-ICP-MS
636 data (Appendix Table S3). The calculated crystallization pressures for the syn-
637 mineralization intrusions from the arc-related Songbei, Yangjiazhangzi and Lanjiagou
638 deposits fall within the range of 1.3 to 3.7 kbar, which is comparable with the results
639 of the syn-mineralization intrusions from the Climax-type Hashitu deposit of 0.7 to
640 2.3 kbar. Taken together, the calculated crystallization pressures for the syn-
641 mineralization intrusions from the Songbei-Yangjiazhangzi-Lanjiagou ore zone and
642 Hashitu deposit are mostly fall within the range of 1.0 to 2.5 kbar (Fig. 8),
643 corresponding to emplacement depths of 3.3 to 8.3 km. This range of values is
644 similar to those reported for other porphyry Mo systems of both arc-related and
645 Climax-type of 1.5 to 6.0 km (e.g., White et al. 1981; Seedorff et al. 2005; Audétat
646 and Li 2017), and all indicate a relatively shallow emplacement depth for causative
647 intrusions, which is consistent with the porphyritic textures of the syn-mineralization
648 intrusions (Fig. 2) and the brittle nature of the molybdenite-bearing stockwork
649 veining in the investigated deposits (Ouyang et al. 2020). The reason for the shallow
650 emplacement depth of syn-mineralization intrusions in porphyry system may lie in
651 the behavior of H₂O, as water solubility in granite melts is strongly pressure, rather
652 than melt composition dependent, with solubility decreasing markedly at pressures
653 below 2.0 kbar (Johannes and Holtz 1996; Burnham 1997). The above evidence
654 suggests that magma emplacement depth most likely plays a fundamental role in the
655 development of porphyry Mo mineralization of both arc-related and Climax-type
656 deposits. As shown in Figure 8, however, no variation in magma emplacement depth

657 is observed between the syn- and pre-mineralization intrusions in the individual
658 deposits investigated here, implying additional factors must also be important.

659 **Influence of magma water content**

660 Based on estimated crystallization temperatures and pressures of melt inclusions
661 from the Climax-type Hashitu and arc-related Yangjiazhangzi deposits ([Appendix](#)
662 [Table S3](#)), and the water solubility models of [Johannes and Holtz \(1996\)](#) and [Holtz et](#)
663 [al. \(2001\)](#), the saturated water contents of ore-forming magmas at Hashitu and
664 Yangjiazhangzi are estimated at 4.2 to 6.2 wt% and 5.1 to 8.6 wt%, respectively.
665 These values are almost identical to those estimated based on melt inclusion EPMA
666 data of 4.4 to 7.8 wt% for Hashitu and 4.6 to 7.4 wt% for Yangjiazhangzi ([Appendix](#)
667 [Table S4](#)), according to the method of [Devine et al. \(1995\)](#). This indicates that the
668 ore-forming magmas at Hashitu and the Songbei-Yangjiazhangzi-Lanjiagou ore zone
669 were all water-saturated and/or supersaturated at their emplacement depths.
670 Similar water-saturated and/or supersaturated ore-forming magmas have also been
671 observed in many other porphyry Mo systems of both arc-related and Climax-type.
672 For example, melt inclusion data show that the ore-forming magmas of the Climax
673 and Urad-Hederson porphyry Mo deposits contain 4.0 to 9.0 wt% H₂O with
674 crystallization pressures of 4.0 to 1.0 kbar ([Fig. 6c](#); [Audétat 2015](#); [Zhang and Audétat](#)
675 [2017](#)), indicating a water-saturated to supersaturated conditions. Does this mean
676 that some intrusions are barren because their magmas are water-undersaturated at
677 their emplacement depths and hence cannot exsolve sufficient volumes of metal-
678 bearing fluids for mineralization? In this study, the water contents of the pre-
679 mineralization intrusions at their emplacement depths could not be estimated
680 directly due to the poor preservation of melt inclusions. However, we consider that
681 the pre-mineralization intrusions were most likely water-saturated, along with their
682 corresponding syn-mineralization intrusions, as the estimated crystallization
683 pressures, zircon Hf isotopic compositions and the bulk compositions of the pre- and
684 syn-mineralization intrusions in the individual deposits are comparable. Hence, it

685 appears that, in addition to melt water content, additional factors may be also
686 critical for the formation of porphyry Mo deposits.

687 **Influence of magma oxygen fugacity**

688 Under oxidized conditions, Mo partitions in favor of the melt over Ti-bearing
689 minerals and thus can enhance the availability of Mo for partitioning into the
690 aqueous phase (Candela and Bouton 1990; Ballard et al. 2002). Hence, oxygen
691 fugacity (fO_2) is considered an important factor affecting the mineralization potential
692 of porphyry Mo systems (e.g., Cerny et al. 2005; Shu et al. 2019). In this study, due to
693 the rare occurrence of magmatic molybdenite in quartz phenocrysts, only the fO_2 of
694 the syn-mineralization granite porphyry from the Climax-type Hashitu deposit was
695 obtained. Based on zircon saturation temperatures of 761 to 785 °C and melt Mo
696 concentrations of 2.5 to 7.0 ppm (Appendix Table S3), using the molybdenite
697 solubility model of Audétat et al. (2011), the calculated magma oxygen fugacity for
698 the syn-mineralization intrusions from the Hashitu deposit ranging from $\Delta FMQ+0.5$
699 to $\Delta FMQ+3.0$ ($\Delta FMQ+1.0$ on average; Fig. 6d). These values broadly overlap with
700 those constrained for Climax-type deposits of $\Delta FMQ=1.5$ to 3.3 (Audétat 2015;
701 Audétat and Li 2017; Zhang and Audétat 2017 and references therein) and for arc-
702 related deposits of $\Delta FMQ=1.8$ to 4.1 (Shu et al. 2019; Xing et al. 2021), all indicative
703 of oxidized conditions. Accordingly, available evidence suggests that oxidized
704 magmas may play a fundamental role in the formation of porphyry Mo deposits of
705 both arc-related and Climax-type.

706 Whole rock major and trace elements and zircon Hf isotope data show that, the
707 pre- and syn-mineralization intrusions in the individual deposits investigated in this
708 study have a common magma source and have experienced a similar petrogenetic
709 evolution (Figs. 3-4). Moreover, petrographic observations show that the pre- and
710 syn-mineralization intrusions in the individual deposits are both characterized by the
711 presence of primary titanite and magnetite, and an absence of ilmenite. Together,
712 this evidence indicates that the pre-mineralization intrusions are most likely oxidized

713 as well as their corresponding syn-mineralization intrusions. As not all of them host
714 Mo mineralization, factors other than magma oxygen fugacity likely control the
715 actual ore-forming event in porphyry Mo systems.

716 **Key processes for the formation of porphyry Mo deposits**

717 The evidence presented in the previous sections suggests that magma emplacement
718 depth, water content and oxygen fugacity play fundamental roles in the genesis of
719 porphyry Mo deposits of both arc-related and Climax-type. However, as not all
720 oxidized, water-saturated magmas emplaced at the favorable depths (i.e., 1.5-6.0 km
721 palaeodepth; [Seedorff et al. 2005](#)) develop fertile magmatic-hydrothermal Mo
722 systems; other factors may therefore be more critical in facilitating the actual ore-
723 forming event in porphyry Mo systems.

724 The Mo-poor characteristics of many ore-forming magmas as shown in the
725 present and previous studies implies that substantial volumes of magma and fluids
726 are required to provide the Mo present in the deposits. For example, assuming the
727 ore-forming magmas have a density of 2.4 g/cm³ ([Fountain and Christensen, 1989](#)), a
728 Mo concentration of 2 ppm, and 100 percent extraction efficiency of Mo from the
729 magma, to account for the 0.26 Mt of Mo present in the Yangjiazhangzi deposit
730 ([Huang et al. 1989](#)), at least 26 km³ of magma is necessary. Meanwhile, at least 2.8
731 km³ of intermediate-density fluids are needed, assuming the fluid contains 100 ppm
732 Mo ([Audétat, 2019](#)) and 100 percent precipitation efficiency of Mo from the fluids.
733 Based on the outcrop area of intrusions and an assumed minimum thickness of 1 km,
734 the constrained volume for the syn-mineralization intrusions in the Yangjiazhangzi
735 deposit total less than 1 km³ ([Fig. 1d](#)), which is significantly smaller than the
736 minimum magma volume (i.e., 26 km³) required for mineralization. On the contrary,
737 the constrained volume for the cogenetic barren intrusions in the Songbei-
738 Yangjiazhangzi-Lanjiagou ore zone is greater than 200 km³ ([Fig. 1b](#)), large enough to
739 produce a giant Mo deposit. The magma volume paradox outlined above indicates
740 that the causative intrusions in porphyry Mo systems may solely act as conduits

741 through which deep seated magmas with fluid and molybdenum cargoes are
742 transferred to the site of mineralization.

743 As shown in [Figure 1](#) and [Appendix Figure 1](#), the pre-mineralization intrusions in
744 the arc-related Songbei-Yangjiazhangzi-Lanjiagou ore zone and Climax-type Hashitu
745 deposit tend to occur as flat, ponded intrusions, whereas the cogenetic syn-
746 mineralization intrusions typically occur as small stocks or dikes intruding into the
747 pre-mineralization intrusions or wall rocks. Moreover, in areas where the syn-
748 mineralization intrusion develops apophyses intruding into the pre-mineralization
749 intrusion, molybdenite mineralization is generally well developed ([Appendix Figure](#)
750 [1](#)). This arrangement indicates that the actual ore-forming event in porphyry Mo
751 systems may be determined by spatial focusing of ore-forming fluids exsolved from
752 the underlying magma chamber. If the fluids vent through flat, ponded intrusions,
753 then the fluid flow may be insufficiently focused to lead to economic ore formation
754 as is considered the case for the Huangshan felsic pluton ([Zhang and Audétat, 2018](#))
755 and the Yerington batholith ([Schöpa et al., 2017](#)). Instead, mineralization may only
756 form when fluids are spatially focused along focusing structures, such as small
757 igneous intrusive bodies. This inference is consistent with the geometries of the
758 porphyry (-skarn) Mo deposits investigated in this and previous studies, which
759 typically exhibit narrow cylindrical or pipe-like forms associated with small stocks or
760 dikes with diameters of less than 500 m (e.g., [Carten et al. 1993](#); [Seedorff and](#)
761 [Einaudi 2004](#); [Gaynor et al. 2019](#); [Ouyang et al. 2021](#); [this study](#)). The typical
762 porphyritic texture of the syn-mineralization intrusions, as shown in [Figure 2](#),
763 suggests that draining magmas and fluids from an underlying magma chamber may
764 be instantaneous (sudden), forceful and voluminous. The rapid release of
765 voluminous fluids has been shown to be key in the development of porphyritic
766 textures ([Nabelek et al. 2010](#)). Such forceful discharge of voluminous fluids is also
767 supported by the development of breccia pipes and stockwork mineralization in the
768 deposits investigated in this study ([Fig. 1e](#); [Appendix Figure 1](#)) and in many other
769 porphyry Mo deposits (e.g., Quartz Hill, [Ashleman et al. 1997](#); Chalukou, [Zhao et al.](#)
770 [2021](#); Luming, [Ouyang et al. 2021](#)). The field evidence presented above indicates

771 that, in porphyry Mo systems, the forceful release of voluminous fluids, the
772 formation of plug-shaped porphyritic intrusions and focused fluid flow may be self-
773 organizational and related. This is because once a steep pressure gradient develops
774 in the upper part of a magma chamber; this site represents the most favorable
775 location for the formation of focusing structures (e.g., plug-shaped intrusions) and
776 voluminous venting of fluids (Castro and Dingwell 2009). Such self-organizational and
777 related events are most likely related a sudden depressurization of the magma
778 chamber as has been previously alluded to in the literature (e.g., Nishimura 2004;
779 Castro and Dingwell 2009; Wotzlaw et al. 2014). Hence, we conclude that the sudden
780 depressurization of the magma chamber and consequent venting of voluminous
781 fluids along focusing structures (e.g., porphyry fingers), appears critical for the
782 formation of porphyry Mo deposits of both arc-related and Climax-type.
783 Determination of the processes responsible for the sudden depressurization of a
784 magma chamber is beyond the scope of this study, however, notably, the most likely
785 mechanisms include over-pressuring of a magma chamber by fluid exsolution during
786 magmatic crystallization (e.g., Stock et al. 2016; Chelle-Michou et al. 2017), seismic
787 shaking (e.g., Avouris et al. 2017), or a combination of the two (e.g., Nishimura 2004,
788 2017).

789 **Implications for the exploration of porphyry Mo deposits**

790 Existing hypotheses for the formation of porphyry Mo deposits broadly follow two
791 distinct lines of argument. One view is that specific magma sources or anomalously
792 Mo-rich compositions are required to form economically significant porphyry Mo
793 deposits (e.g., Pettke et al. 2010; Xie et al. 2017). In this scenario, parental magmas
794 from the metasomatized mantle or lower crust are thought to be enriched in Mo
795 from the outset. Empirical evidence for a source control includes the observation
796 that some regions of the Earth, e.g., Colorado Mineral Belt of Western North
797 American, Qinling-Dabie orogen of Central China and northeastern China, seem
798 particularly well endowed with porphyry Mo deposits. An alternative view, however,

799 suggests that porphyry Mo mineralization is caused by specific magmas with normal
800 Mo contents and elevated oxygen fugacity and water contents (e.g., [Shu et al. 2019](#);
801 [Xing et al. 2021](#)). If source characteristics are essential for the formation of porphyry
802 Mo deposits, the potential of finding new mineral resources would be largely limited
803 to specific provinces or regions. Alternatively, if specific magmas alone can account
804 for the formation of porphyry Mo deposits, any area with suitable magmas (i.e.,
805 elevated oxygen fugacity and water content) could become a target for exploration.

806 The results presented in this study suggest that unique magma sources are not
807 required for the formation of porphyry Mo deposits of both arc-related and Climax-
808 type. Although the two classes of porphyry Mo deposits were formed in distinct
809 tectonic settings and are associated with different kinds of intrusions, their
810 formation is fundamentally controlled by similar geological processes and/or factors.
811 A prerequisite for the formation of porphyry Mo deposits of both arc-related and
812 Climax-type is the emplacement of oxidized, water-saturated magmas at 1.5 to 6.0
813 km palaeodepth. However, the actual ore-forming event itself is considered to relate
814 to a sudden depressurization of the magma chamber and consequent venting of
815 voluminous fluids along focusing structures, such as small stocks or dike swarms.

816 The tectonic setting and everything that relates to the evolution of the magma
817 through to fluid saturation, emplacement of porphyries, and vein formation of the
818 four selected deposits in this study are absolutely typical of the end members of
819 porphyry Mo family. As such, the conclusions of this work are potentially of utmost
820 importance for exploration as they suggest fluid processes in the shallow crust are
821 crucial for the formation of both arc-related and Climax-type porphyry Mo deposits.
822 Meanwhile, we also infer that any area with a suitable magmatic-hydrothermal
823 architecture could become a target for exploration of porphyry Mo deposits. Hence,
824 it appears that the most important factors for the creation of porphyry deposits is
825 the consolidation of an optimal combination of geometry, size, emplacement level
826 and particularly the roof shape of big granite plutons (i.e., magma chambers) that
827 are coeval with mineralization. For these reasons, geophysical methods that relate
828 directly to the geometry of magma chambers, such as seismic reflection and

829 geomagnetic and gravity surveys, likely constitute the single most important tools in
830 the uncovering of hidden porphyry deposits.

831 **Acknowledgments**

832 This research is supported by National Key R&D Plan (Grant No. 2017YFC0601403),
833 Scientific Research Fund of the China Central Non-Commercial Institute (No. KK2013)
834 and International Postdoctoral Exchange Fellowship Program of China Postdoctoral
835 Council (No. 20170032). We sincerely thank Detlef Krause for help with the
836 microprobe analyses and Raphael Njul for the excellent polishing work. We
837 particularly thank Andreas Audétat for helping with sampling and melt inclusion LA-
838 ICP-MS analyses. Constructive comments from three anonymous reviewers are
839 greatly appreciated, together with the thorough editorial handling of associate editor
840 Julie Roberge.

841 **References**

- 842 Ashleman, J.C., Taylor, C.D., and Smith, P.R. (1997) Porphyry molybdenum deposits
843 of Alaska, with emphasis on the geology of the Quartz Hill deposit, southeastern
844 Alaska. *Economic Geology*, 9, 334-354.
- 845 Audétat, A. (2010) Source and evolution of molybdenum in the porphyry Mo (-Nb)
846 deposit at Cave Peak, Texas. *Journal of Petrology*, 51, 1739-1760.
- 847 Audétat, A., Dolejs, D., and Lowenstern, J.B. (2011) Molybdenite saturation in silicic
848 magmas, occurrence and petrological implications. *Journal of Petrology*, 52,
849 891-904.
- 850 Audétat, A. (2015) Compositional evolution and formation conditions of magmas and
851 fluids related to porphyry Mo mineralization at Climax, Colorado. *Journal of*
852 *Petrology*, 56, 1519-1546.
- 853 Audétat, A., and Li, W.T. (2017) The genesis of Climax-type porphyry Mo deposits,
854 insights from fluid inclusions and melt inclusions. *Ore Geology Reviews*, 88, 436-
855 460.

- 856 Audétat, A. (2019). The metal content of magmatic-hydrothermal fluids and its
857 relationship to mineralization potential. *Economic Geology*, 114, 1033-1056.
- 858 Avouris, D.M., Carn, S.A., and Waite, G.P. (2017) Triggering of volcanic degassing by
859 large earthquakes. *Geology*, 45, 715-718.
- 860 Ballard, J.R., Palin, M.J., and Campbell, I.H. (2002) Relative oxidation states of
861 magmas inferred from Ce(IV)/Ce(III) in zircon: Application to porphyry copper
862 deposits of northern Chile. *Contributions to Mineralogy and Petrology*, 144,
863 347-364.
- 864 Blichert-Toft, J., and Albarède, F. (1997) The Lu-Hf isotope geochemistry of
865 chondrites and the evolution of the mantle-crust system. *Earth and Planetary
866 Science Letters*, 148, 243-258.
- 867 Blichert-Toft, J., Chauvel, C., and Albarède, F. (1997) Separation of Hf and Lu for high-
868 precision isotope analysis of rock samples by magnetic sector-multiple collector
869 ICP-MS. *Contributions to Mineralogy and Petrology*, 127, 248-260.
- 870 Burnham, C.W. (1997) *Geochemistry of hydrothermal ore deposits*, 670 p. Wiley,
871 New York.
- 872 Candela, P.A., and Bouton, S.L. (1990) The influence of oxygen fugacity on tungsten
873 and molybdenum partitioning between silicate melts and ilmenite. *Economic
874 Geology*, 85, 633-640.
- 875 Carten, R.B., White, W.H., and Stein, H.J. (1993) High-grade granite-related
876 molybdenum systems: Classification and origin. In Kirkham, R.V., Sinclair, W.D.,
877 Thorpe, R.I., and Duke, J.M. Eds., *Mineral Deposit Modeling*, 40, p. 521-554.
878 Geological Association of Canada, Special Paper, United States of Geological
879 Survey, Reston, Virginia.
- 880 Castro, J.M., and Dingwell, D.B. (2009) Rapid ascent of rhyolitic magma at Chaiten
881 volcano, Chile. *Nature*, 461, 780-783.
- 882 Cerny, P., Blevin, P.L., Cuney, M., and London, D. (2005) Granite-related ore
883 deposits. *Society of Economic Geologists*, 100, 337-370.

- 884 Chelle-Michou, C., Rottier, B., Caricchi, L., and Simpson, G. (2017) Tempo of magma
885 degassing and the genesis of porphyry copper deposits. Scientific reports,
886 doi.org/10.1038/srep40566.
- 887 Chen, B., Zhai, M.G., and Tian, W. (2007) Origin of the Mesozoic magmatism in the
888 North China Craton, constraints from petrological and geochemical data.
889 Geological Society, London, Special Publications, 280, 131-151.
- 890 Chen, Y.J., Zhang, C., Wang, P., Pirajno, F., and Li, N. (2017) The Mo deposits of
891 northeast China: a powerful indicator of tectonic settings and associated
892 evolutionary trends. *Ore Geology Reviews*, 81, 602-640.
- 893 Chu, S.X., Zeng, Q.D., and Liu, J.M. (2017) Re-Os and U-Pb geochronology of the
894 Songbei porphyry-skarn Mo deposit, North China Craton, Implications for the
895 Early Jurassic tectonic setting in eastern China. *Journal of Geochemical*
896 *Exploration*, 181, 256-269.
- 897 Cui, Y. B. (2019) Study on buried granite and its contact metamorphism in
898 Yangjiazhangzi, western Liaoning province. Jiling University, 45.
- 899 Devine, J.D., Gardner, J.E., Brack, H.P., Laynet, G.D., and Rutherford, M.J. (1995)
900 Comparison of microanalytical methods for estimating H₂O contents of silicic
901 volcanic glasses. *American Mineralogist*, 80, 319-328.
- 902 Dilles, J.H. (1987) Petrology of the Yerington batholith, Nevada: Evidence for
903 evolution of porphyry copper ore fluids. *Economic Geology*, 82, 1750-1789.
- 904 Dingwell, D.B., Scarfe, M.C., and Cronin, D.J. (1985) The effect of fluorine on
905 viscosities in the system Na₂O-Al₂O₃-SiO₂: Implications for phonolites, trachytes
906 and rhyolites. *American Mineralogist*, 70, 80-87.
- 907 Donovan, J., and Vicenzi, E. (2008) Water by EPMA-new developments. *Microscopy*
908 *and Microanalysis*, [doi,10.1017/s1431927608082615](https://doi.org/10.1017/s1431927608082615).
- 909 Fountain, D.M., and Christensen, N.I. (1989) Composition of the continental crust
910 and upper mantle: A review: Geophysical Framework of the Continental United
911 States, 172, 711-742.

- 912 Gaynor, S.P., Rosera, J.M., and Coleman, D.S. (2019) Intrusive history of the
913 Oligocene Questa porphyry molybdenum deposit, New Mexico. *Geosphere*, 15,
914 548-575.
- 915 Ge, W.C., Wu, F.Y., Zhou, C.Y., and Zhang, J.H. (2007) Porphyry Cu-Mo deposits in the
916 eastern Xing'an-Mongolian orogenic belt: Mineralization ages and their
917 geodynamic implications. *Chinese Science Bulletin*, 52, 3416-3427.
- 918 Goldfarb, R.J., Mao, J.W., Qiu, K.F., and Goryachev, N. (2021) The great Yanshanian
919 metallogenic event of eastern Asia: Consequences from one hundred million
920 years of plate margin geodynamics. *Gondwana Research*,
921 <https://doi.org/10.1016/j.gr.2021.02.020>.
- 922 Griffin, W.L., Pearson, N.J., Belousova, E., Jackson, S.E., Van Acherbergh, E., O'Reilly
923 S.Y., and Shee, S.R. (2000) The Hf isotope composition of cratonic mantle, LAM-
924 MC-ICPMS analysis of zircon megacrysts in kimberlites. *Geochimica et*
925 *Cosmochimica Acta*, 64, 133-147.
- 926 Griffin, W.L., Wang, X., Jackson, S.E., Pearson, N., O'Reilly, S.Y., Xu, X.S., Zhou, X.M.
927 (2002) Zircon chemistry and magma mixing, SE China, in-situ analysis of Hf
928 isotopes, Tonglu and Pingtan igneous complexes. *Lithos*, 6, 237-269.
- 929 Han, C.M., Xiao, W.J., Zhao, G.C., Sun, M., Qu, W.J., and Du, A.D. (2009) A Re-Os
930 study of molybdenites from the Lanjiagou Mo deposit of North China Craton
931 and its geological significance. *Gondwana Research*, 16, 264-271.
- 932 Holtz, F., Johannes, W., Tamic, N., and Behrens, H. (2001) Maximum and minimum
933 water contents of granitic melts generated in the crust: A reevaluation and
934 implications. *Lithos*, 56, 1-14.
- 935 Huang, D.H., Dong, Q.Y., and Gan, Z.X. (1989) China molybdenum deposits. In Song
936 S.H., Eds., *China Deposits*, 1, pp, 493-536. Geology Publishing House, Beijing (in
937 Chinese).
- 938 Huang, D.H., Wu, C.Y., Du, A.D., He, H.L. (1994) Re-Os ages molybdenum deposits in
939 east Qinling and their significance. *Mineral Deposits*, 13, 221-230 (in Chinese).

- 940 Huang, R., and Audétat, A. (2012) The titanium-in-quartz (TitaniQ)
941 thermobarometer: A critical examination and re-calibration. *Geochimica et*
942 *Cosmochimica Acta*, 84, 75-89.
- 943 Irvine, T.N.J., and Baragar, W.R.A. (1971) A guide to the chemical classification of the
944 common volcanic rocks. *Canadian journal of earth sciences*, 8, 523-548.
- 945 Ishihara, S., and Shibata, K. (1980) Mineralization age of the Yangjiazhangzi
946 molybdenum deposits, China. *Mining Geology*, 30, 27-29.
- 947 Jiang, N., Zhang, S.Q., Zhou, W., and Liu, Y.S. (2009). Origin of a Mesozoic granite
948 with A-type characteristics from the North China craton: highly fractionated
949 from I-type magmas? *Contributions to Mineralogy and Petrology*, 158(1), 113-
950 130.
- 951 Johannes, W., and Holtz, F. (1996) Petrogenesis and experimental petrology of
952 granitic rocks, 335 p. Springer, Berlin, Heidelberg.
- 953 Keith, J.D., Christiansen, E.H., and Carten, R.B. (1993) The genesis of giant porphyry
954 molybdenum deposits. Society of Economic Geologists. Book Chapter. Book
955 Title: Giant Ore Deposits. 285-317.
- 956 Keppler, H., and Wyllie, P.J. (1991) Partitioning of Cu, Sn, Mo, W, U, and Th between
957 melt and aqueous fluid in the systems haplogranite-H₂O-HCl and haplogranite-
958 H₂O-HF. *Contributions to Mineralogy and Petrology*, 109(2), 139-150.
- 959 Le Bas, M.J., Maitre, R.W.L., Streckeisen, A., and Zanettin, B. (1986) A chemical
960 classification of volcanic rocks based on the total alkali-silica diagram. *Journal of*
961 *Petrology*, 27, 745-750.
- 962 Lerchbaumer, L., and Audétat, A. (2013) The metal content of silicate melts and
963 aqueous fluids in subeconomically Mo mineralized granites: Implications for
964 porphyry Mo genesis. *Economic Geology*, 108, 987-1013.
- 965 Liu, J.F., Li, J.Y., Chi, X.G., Zheng, P.X., Hu, Z.C., and Zhang, X.W. (2020) Destruction of
966 the northern margin of the North China Craton in Mid-Late Triassic: Evidence
967 from asthenosphere-derived mafic enclaves in the Jiefangyingzi granitic pluton
968 from the Chifeng area, southern Inner Mongolia. *Acta Geologica Sinica (English*
969 *Edition)*, 94(4): 1071–1092.

- 970 Lowenstern, J.B. (1994) Dissolved volatile concentrations in an ore-forming
971 magma. *Geology*, 22, 893-896.
- 972 Ludington S., and Plumlee G.S. (2009) Climax-type porphyry molybdenum deposits.
973 16 p. U.S. Geological Survey, Reston, Virginia.
- 974 McCulloch, M.T., Rosman, K.J., and De Laeter, J.R. (1977) The isotopic and elemental
975 abundance of ytterbium in meteorites and terrestrial samples. *Geochimica et*
976 *Cosmochimica Acta*, 41, 1703-1707.
- 977 Meng, Q.R. (2003) What drove late Mesozoic extension of the northern China-
978 Mongolia tract? *Tectonophysics*, 369, 155-174.
- 979 Nabelek, P.I., Whittington, A.G., and Sirbescu, M.L.C. (2010) The role of H₂O in rapid
980 emplacement and crystallization of granite pegmatites, resolving the paradox of
981 large crystals in highly undercooled melts. *Contributions to Mineralogy and*
982 *Petrology*, 160, 313-325.
- 983 Nishimura, T. (2004) Pressure recovery in magma due to bubble growth. *Geophysical*
984 *research letters*, doi,10.1029/2004gl019810.
- 985 Nishimura, T. (2017) Triggering of volcanic eruptions by large earthquakes.
986 *Geophysical Research Letters*, 44, 7750-7756.
- 987 Ouyang, H.G., Mao, J.W., Santosh, M., Zhou, J., Zhou, Z.H., Wu, Y., and Hou, L. (2013)
988 Geodynamic setting of Mesozoic magmatism in NE China and surrounding
989 regions, perspectives from spatio-temporal distribution patterns of ore
990 deposits. *Journal of Asian Earth Sciences*, 78, 222-236.
- 991 Ouyang, H.G., Mao, J.W., and Hu, R.Z. (2020) Geochemistry and crystallization
992 conditions of magmas related to porphyry Mo mineralization in northeastern
993 China. *Economic Geology*, 115, 79-100.
- 994 Ouyang, H.G., Mao, J.W., Hu, R.Z., Caulfield, J., and Zhou, Z.H. (2021) Controls on the
995 metal endowment of porphyry Mo deposits: Insights from the Luming porphyry
996 Mo deposit, northeastern China. *Economic Geology*, [https://doi.org/](https://doi.org/10.5382/econgeo.4850)
997 [10.5382/econgeo.4850](https://doi.org/10.5382/econgeo.4850).

- 998 Pettke, T., Oberli, F., and Heinrich, C.A. (2010) The magma and metal source of giant
999 porphyry-type ore deposits, based on lead isotope microanalysis of individual
1000 fluid inclusions. *Earth and Planetary Science Letters*, 296, 267-277.
- 1001 Richards, J.P. (2011a) Magmatic to hydrothermal metal fluxes in convergent and
1002 collided margins. *Ore Geology Reviews*, 40, 1-26.
- 1003 Richards, J.P. (2011b) High Sr/Y arc magmas and porphyry Cu±Mo±Au deposits: just
1004 add water. *Economic Geology*, 106, 1075-1081.
- 1005 Romick, J.D., Kay, S.M., and Kay, R.W. (1992) The influence of amphibole
1006 fractionation on the evolution of calc-alkaline andesite and dacite tephra from
1007 the central Aleutians, Alaska. *Contributions to Mineralogy and Petrology*, 112,
1008 101-118.
- 1009 Schöpa, A., Annen, C., Dilles, J.H., Sparks, R.S.J., and Blundy, J.D. (2017) Magma
1010 emplacement rates and porphyry copper deposits: Thermal modeling of the
1011 Yerington Batholith, Nevada. *Economic Geology*, 112, 1653-1672.
- 1012 Seedorff, E., and Einaudi, M.T. (2004) Henderson porphyry molybdenum system,
1013 Colorado, I. Sequence and abundance of hydrothermal mineral assemblages,
1014 flow paths of evolving fluids, and evolutionary style. *Economic Geology*, 99, 3-
1015 37.
- 1016 Seedorff, E., Dilles, J.H., Proffett, J.M., Jr., Einaudi, M.R., Zurcher, L., Stavast, W.J.A.,
1017 Johnson, D.A., and Barton, M.D. (2005) Porphyry copper deposits:
1018 Characteristics and origin of hypogene features. In J.W. Hedenquist, J.F.H.
1019 Thompson, R.J. Goldfarb, and J.P. Richards, Eds., *Economic Geology and Bulletin*
1020 *of the Society of Economic Geologists One Hundredth Anniversary Volume*
1021 *1905-2005*, p. 251-298. Society of Economic Geologists, Littleton, Colorado.
- 1022 Shu, Q.H., Chang, Z.S., Lai, Y., Zhou, Y.T., Sun, Y., and Yan, C. (2016) Regional
1023 metallogeny of Mo-bearing deposits in northeastern China, with new Re-Os
1024 dates of porphyry Mo deposits in the northern Xilamulun district. *Economic*
1025 *Geology*, 111, 1783–1798.

- 1026 Shu, Q.H., Chang, Z.S., Lai, Y., Hu, X., Wu, H., Zhang, Y., Wang, P., Zhai, D.G., and
1027 Zhang, C. (2019) Zircon trace elements and magma fertility, insights from
1028 porphyry (-skarn) Mo deposits in NE China. *Mineralium Deposita*, 54, 645-656.
- 1029 Shu, Q.H., and Chiaradia, M. (2021) Mesozoic Mo mineralization in northeastern
1030 China did not require regional-scale pre-enrichment. *Economic Geology*,
1031 <https://doi.org/10.5382/econgeo.4823>.
- 1032 Sláma, J., Košler, J., Condon, D.J., Crowley, J.L., Gerdes, A., Hanchar, J.M., Horstwood,
1033 M.S., Morris, G.A., Nasdala, L., and Norberg, N. (2008) Plešovice zircon-a new
1034 natural reference material for U-Pb and Hf isotopic microanalysis. *Chemical*
1035 *Geology*, 249, 1-35.
- 1036 Söderlund, U., Patchett, P.J., Vervoort, J.D., and Isachsen, C.E. (2004) The ¹⁷⁶Lu decay
1037 constant determined by Lu-Hf and U-Pb isotope systematics of Precambrian
1038 mafic intrusions. *Earth and Planetary Science Letters*, 219, 311-324.
- 1039 Stein, H.J., and Hannah, J.L. (1985) Movement and origin of ore fluids in Climax-type
1040 systems. *Geology*, 13, 469-474.
- 1041 Stock, M.J., Humphreys, M.C., Smith, V.C., Isaia, R., and Pyle, D.M. (2016) Late-stage
1042 volatile saturation as a potential trigger for explosive volcanic eruptions. *Nature*
1043 *Geoscience*, 9, 249-254.
- 1044 Sun, S.S., and McDonough, W.F. (1989) Chemical and isotopic systematics of oceanic
1045 basalts, implications for mantle composition and processes. Geological Society,
1046 London, Special Publications, 42, 313-345.
- 1047 Taylor, R.D., Hammarstrom, J.M., Piatak, N.M., and Seal, R.R. (2012) Arc-related
1048 porphyry molybdenum deposit model, 64 p. U.S. Geological Survey, Reston,
1049 Virginia.
- 1050 Webster, J.D. (1997). Chloride solubility in felsic melts and the role of chloride in
1051 magmatic degassing. *Journal of petrology*, 38(12), 1793-1807.
- 1052 Whalen, J.B., Currie, K.L., and Chappell, B.W. (1987) A-type granites, geochemical
1053 characteristics, discrimination and petrogenesis. *Contributions to mineralogy*
1054 *and petrology*, 95(4), 407-419.

- 1055 Whalen, J.B., Anderson, R.G., Struik, L.C., and Villeneuve, M.E. (2001) Geochemistry
1056 and Nd isotopes of the François Lake plutonic suite, Endako batholith, host and
1057 progenitor to the Endako molybdenum camp, central British Columbia. Canada
1058 Journal of Earth Science, 38, 603-618.
- 1059 White, W.H., Bookstrom, A.A., Kamilli, R.J., Ganster, M.W., Smith, R.P., and Ranta,
1060 D.E., Steininger, R.C. (1981) Character and origin of Climax-type molybdenum
1061 deposits. Economic Geology, 75th Anniversary Volume, 270-316.
- 1062 Windley, B.F., Alexeiev, D., Xiao, W.J., Kröner, A., and Badarch, G. (2007) Tectonic
1063 models for accretion of the Central Asian Orogenic Belt. Journal of the
1064 Geological Society, 164, 31-47.
- 1065 Wotzlaw, J.F., Bindeman, I.N., Watts, K.E., Schmitt, A.K., Caricchi, L., and Schaltegger,
1066 U. (2014) Linking rapid magma reservoir assembly and eruption trigger
1067 mechanisms at evolved Yellowstone-type supervolcanoes. Geology, 42, 807-
1068 810.
- 1069 Wu, L.R., Zhang, X.Q., and Sun, S.H. (1990) On the magma generation, evolution and
1070 molybdenum mineralization of the Yangjiazhangzi complex, Jinxi, Liaoning
1071 province. Acta Petrologica Sinica, 3, 1-11 (in Chinese).
- 1072 Wu, F.Y., Sun, D.Y., Li, H.M., Jahn, B.M., and Wilde, S. (2002) A-type granites in
1073 northeastern China: age and geochemical constraints on their
1074 petrogenesis. Chemical Geology, 187(1-2), 143-173.
- 1075 Wu, F.Y., Jahn, B.M., Wilde, S.A., Lo, C.H., Yui, T.F., Lin, Q, Ge, W.C., and Sun, D.Y.
1076 (2003) Highly fractionated I-type granites in NE China (II): isotopic geochemistry
1077 and implications for crustal growth in the Phanerozoic. Lithos, 67(3-4), 191-204.
- 1078 Wu, F.Y., Lin, J.Q., Wilde, S.A., Zhang, X.O., and Yang, J.H. (2005) Nature and
1079 significance of the Early Cretaceous giant igneous event in eastern China. Earth
1080 and Planetary Science Letters, 233, 103-119.
- 1081 Wu, F.Y., Yang, J.H., Zhang, H.B., and Liu, X.M. (2006) Emplacement ages of the
1082 Mesozoic granites in southeastern part of the Western Liaoning Province. Acta
1083 Petrologica Sinica, 22, 315-325.

- 1084 Wu, F.Y., Sun, D.Y., Ge, W.C., Zhang, Y.B., Grant, M.L., Wilde, S.A., and Jahn, B.M.
1085 (2011) Geochronology of the Phanerozoic granitoids in northeastern China.
1086 Journal of Asian Earth Sciences, 41, 1-30.
- 1087 Wu, F.Y., Liu, X.C., Ji, W.Q., Wang, J.M., and Yang, L. (2017) Highly fractionated
1088 granites: Recognition and research. Science China Earth Sciences, 60, 1201-
1089 1219.
- 1090 Xiao, W.J., Windley, B.F., Hao, J., and Zhai, M.G. (2003) Accretion leading to collision
1091 and the Permian Solonker suture, Inner Mongolia, China, termination of the
1092 central Asian orogenic belt. Tectonics, doi, 10.1029/2002TC001484.
- 1093 Xie, G.Q., Mao, J.W., Wang, R.T., Meng, D.M., Sun, J., Dai, J.Z., Ren, T., Li, J.B., and
1094 Zhao, H.J. (2017) Origin of the Lengshuigou porphyry-skarn Cu deposit in the
1095 Zha-Shan district, South Qinling, central China, and implications for differences
1096 between porphyry Cu and Mo deposits. Mineralium Deposita, 52, 621-639.
- 1097 Xing, K., Shu, Q.H., and Lentz, D.R. (2021) Constraints on the formation of the giant
1098 Daheishan porphyry Mo deposit (NE China) from whole-rock and accessory
1099 mineral geochemistry. Journal of Petrology, doi: 10.1093/petrology/egab018.
- 1100 Xu, W.L., Gao, S., Wang, Q.H., Wang, D.Y., and Liu, Y.S. (2006) Mesozoic crustal
1101 thickening of the eastern North China craton: Evidence from eclogite xenoliths
1102 and petrologic implications. Geology, 34, 721-724.
- 1103 Xu, W.L., Pei, F.P., Wang, F., Meng, E., Ji, W.Q., and Yang, D.B. (2013) Spatial-
1104 temporal relationships of Mesozoic volcanic rocks in NE China, constraints on
1105 tectonic overprinting and transformations between multiple tectonic regimes.
1106 Journal of Asian Earth Sciences, 74, 167-193.
- 1107 Yuan, H.L., Gao, S., Dai, M.N., Zong, C.L., Günther, D., Fontaine, G.H., Liu, X.M., and
1108 Diwu, C.R. (2008) Simultaneous determinations of U–Pb age, Hf isotopes and
1109 trace element compositions of zircon by excimer laser-ablation quadrupole and
1110 multiple-collector ICP-MS. Chemical Geology, 247, 100-118.
- 1111 Zeng, Q.D., Liu, J.M., Qin, K.Z., Fan, H.R., Chu, S.X., Wang, Y.B., and Zhou, L.L. (2013)
1112 Types, characteristics, and time-space distribution of molybdenum deposits in
1113 China. International Geology Review, 55, 1311-1358.

- 1114 Zhai, D.G., Liu, J.J., Wang, J.P., Yang, Y.Q., Zhang, H.Y., Wang, X.L., Zhang, Q.B., Wang,
1115 G.W., and Liu, Z.J. (2014) Zircon U-Pb and molybdenite Re-Os geochronology,
1116 and whole-rock geochemistry of the Hashitu molybdenum deposit and host
1117 granitoids, Inner Mongolia, NE China. *Journal of Asian Earth Sciences*, 79, 144-
1118 160.
- 1119 Zhai, D.G., Liu, J.J., Tombros, S., and Williams-Jones, A.E. (2018) The genesis of the
1120 Hashitu porphyry molybdenum deposit, Inner Mongolia, NE China, constraints
1121 from mineralogical, fluid inclusion, and multiple isotope (H, O, S, Mo, Pb)
1122 studies. *Mineralium Deposita*, 53, 377-397.
- 1123 Zhao, Q.Q., Zhai, D.G., Mathur, R., Liu, J.J., Selby, D., and Williams-Jones, A.E. (2021)
1124 The giant Chalukou porphyry Mo deposit, northeast China: The product of a
1125 short-lived, high flux mineralizing event. *Economic Geology*,
1126 <https://doi.org/10.5382/econgeo.4818>.
- 1127 Zhang, K., Nie, F.J., Hou, W.R., Li, C., and Liu, Y. (2012) Re-Os isotopic age dating of
1128 molybdenite separates from Hashitu Mo deposit in Linxi County of Inner
1129 Mongolia and its geological significance. *Mineral Deposits*, 31, 129-138.
- 1130 Zhang, D.H., and Audétat, A. (2017) Chemistry, mineralogy and crystallization
1131 conditions of porphyry Mo-forming magmas at Urad-Henderson and Silver
1132 Creek, Colorado, USA. *Journal of Petrology*, 58, 277-296.
- 1133 Zhang, D.H., and Audétat, A. (2018) Magmatic-hydrothermal evolution of the barren
1134 Huangshan pluton, Anhui province, China: A melt and fluid inclusion study.
1135 *Economic Geology*, 113, 803-824.
- 1136 Zhang, Q., Liang, C.Y., Liu, Y.J., Zheng, C.Q., and Li, W.M. (2019) Final closure time of
1137 the Paleo-Asian Ocean: Implication from the provenance transformation from
1138 the Yangjiagou Formation to Lujiatun Formation in the Jiutai area, NE China.
1139 *Acta Geologica Sinica (English Edition)*, 93: 1456–1476.
- 1140 Zheng, Y.C., Feng, H., Wu, C.Z., Gu, L.X., Liu, S.H., and He, K. (2014) Influence of crude
1141 oil on the genesis of the Lanjiagou porphyry molybdenum deposit, western
1142 Liaoning Province, China. *Ore Geology Reviews*, 60, 1-13.
- 1143

1144

Figure captions

1145 Figure 1. (a) Simplified geological map of northeastern China, showing the main
1146 tectonic units and deposits investigated in this study; (b) Simplified geological map of
1147 the area around the Yangjiazhangzi, Lanjiagou and Songbei deposits ([modified from](#)
1148 [Wu et al. 1990](#)); (c) Geological map and cross-section of Songbei ([Chu et al. 2017](#)); (d)
1149 Geological map of Yangjiazhangzi ([Han et al. 2009](#)); (e) Geological map of Lanjiagou
1150 ([Han et al. 2009](#)); (f) Simplified geological map of Hashitu ([Zhai et al. 2018](#)).

1151

1152 Figure 2. Photographs of polished thick sections and melt inclusions in quartz. (a)
1153 Songbei syn-mineralization rhyolite porphyry; (b) Yangjiazhangzi pre-mineralization
1154 granite porphyry; (c) Yangjiazhangzi syn-mineralization rhyolite porphyry; (d) Finely
1155 crystallized melt inclusions in samples from the Songbei deposit; (e-f) Finely
1156 crystallized to glassy melt inclusions from the Yangjiazhangzi syn-mineralization
1157 intrusions; (g) Lanjiagou fine-grained syenogranite; (h) Hashitu pre-mineralization
1158 porphyritic monzogranite; (i) Hashitu syn-mineralization rhyolite porphyry; (j)
1159 Decrepitated, finely crystallized melt inclusions from the Lanjiagou fine-grained
1160 syenogranite; (k) Coarsely crystallized melt inclusions from the Hashitu pre-
1161 mineralization intrusion; (l) Partly crystallized melt inclusions from the Hashitu syn-
1162 mineralization intrusion. Afs = alkali feldspar, Qtz = quartz.

1163

1164 Figure 3. (a) Total alkalis ($\text{Na}_2\text{O}+\text{K}_2\text{O}$) versus SiO_2 diagram (TAS; [Le Bas et al. 1986](#))
1165 and (b) K_2O versus SiO_2 diagram showing the geochemical classification of the whole-
1166 rock samples from the deposits investigated in this study. The dashed line separating
1167 alkaline series from subalkaline series is from [Irvine and Baragar \(1971\)](#); (c-d)
1168 Primitive mantle-normalized trace element diagram and chondrite-normalized REE
1169 patterns for samples from the Hashitu deposit; (e-f) Primitive mantle-normalized
1170 trace element diagram and chondrite-normalized REE patterns for samples from the
1171 Songbei-Yangjiazhangzi-Lanjiagou ore zone; Normalized values from [Sun and](#)
1172 [McDonough \(1989\)](#).

1173

1174 Figure 4. Initial zircon Hf isotopic compositions of the pre- and syn-mineralization
1175 intrusions at their crystallization ages from the Songbei-Yangjiazhangzi-Lanjiagou ore
1176 zone and Hashitu deposit. CHUR=chondritic uniform reservoir mantle.

1177

1178 Figure 5. Cesium concentrations versus (a) Rb concentrations and (b) Mo
1179 concentrations in melt inclusions analyzed in the present study. The Cs, Rb and Mo
1180 concentrations (c-d) in melt inclusions analyzed from Climax-type porphyry Mo
1181 deposits ([Audétat 2015](#); [Audétat and Li 2017](#); [Zhang and Audétat 2017](#)), arc-related
1182 porphyry Mo deposits ([Lerchbaumer and Audétat 2013](#); [Ouyang et al. 2021](#)) and
1183 Huangshan barren granites ([Zhang and Audétat 2018](#)) are shown for comparison.

1184

1185 Figure 6. (a) Fluorine, (b) Cl, (c) H₂O contents and (d) oxygen fugacities of the ore-
1186 forming magmas relating to the deposits investigated in this study and the arc-
1187 related and Climax-type Mo deposits. Data sourced from [Audétat \(2015\)](#), [Audétat](#)
1188 [and Li \(2017\)](#), [Zhang and Audétat \(2017\)](#), [Shu et al. \(2019\)](#) and [Xing et al. \(2021\)](#).

1189

1190 Figure 7. Melt Mo content versus (a) grade and (b) reserve for deposits in this study
1191 and the arc-related and Climax-type deposits. Data sourced from [Carten et al.](#)
1192 [\(1993\)](#); [Audétat \(2015\)](#), [Audétat and Li \(2017\)](#), [Zhang and Audétat \(2017\)](#), and
1193 [Ouyang et al. \(2021\)](#).

1194

1195 Figure 8. Relationship between entrapment pressures (P) and zircon saturation
1196 temperatures (T) of the melt inclusions from the pre- and syn-mineralization
1197 intrusions of the Songbei-Yangjiazhangzi-Lanjiagou ore zone and the Hashitu deposit.

1198

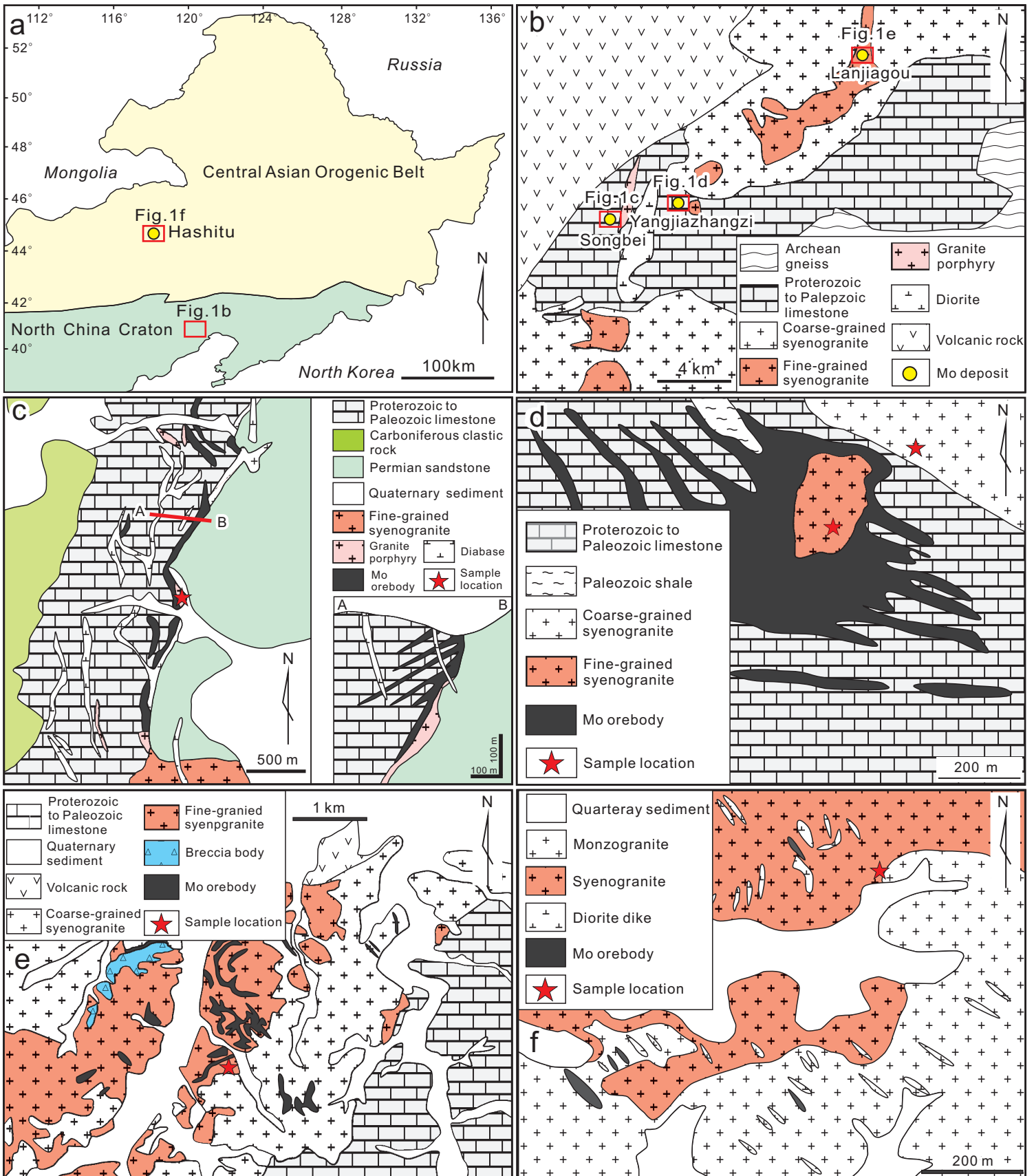
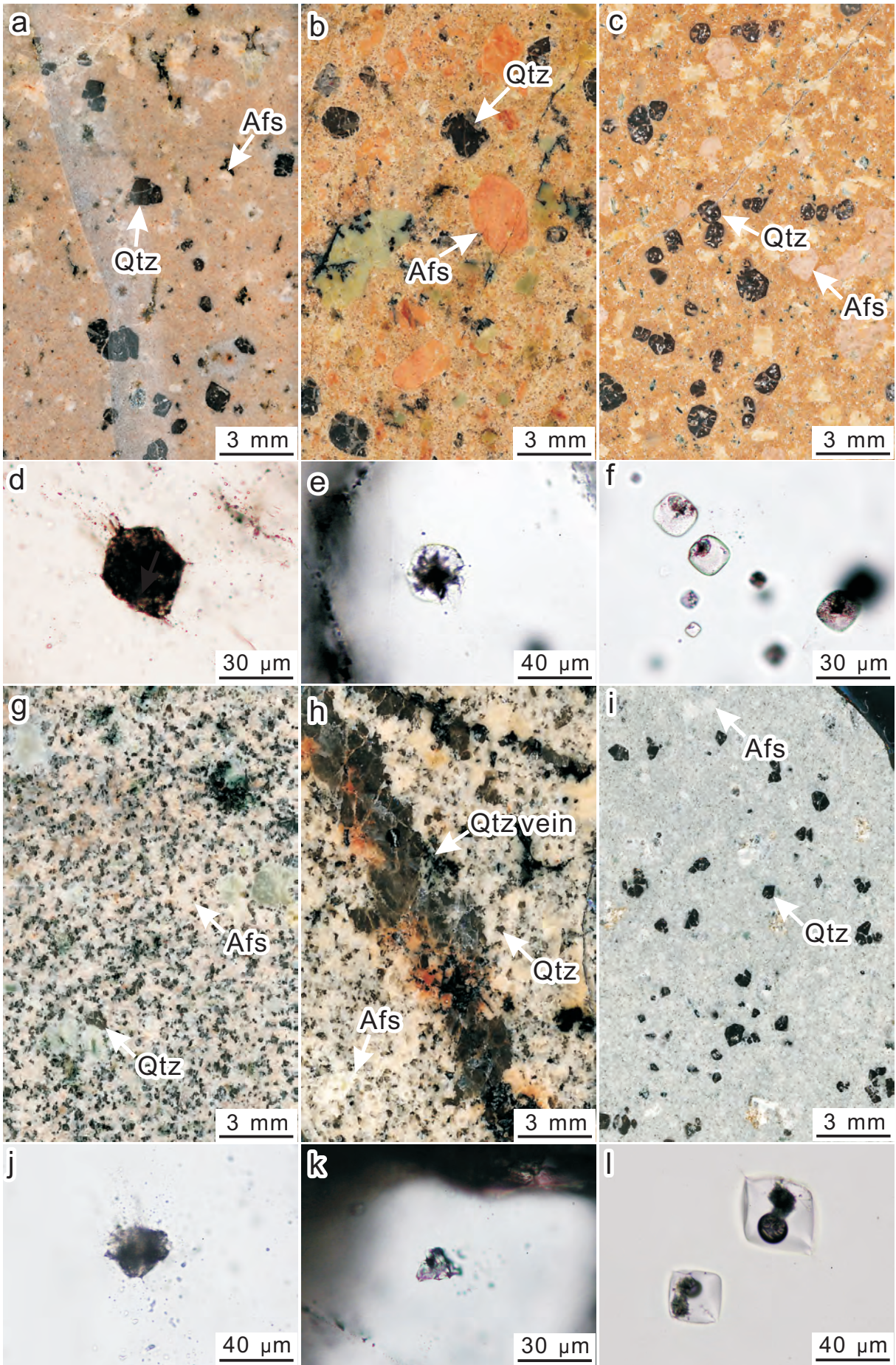


Fig 1



Fig

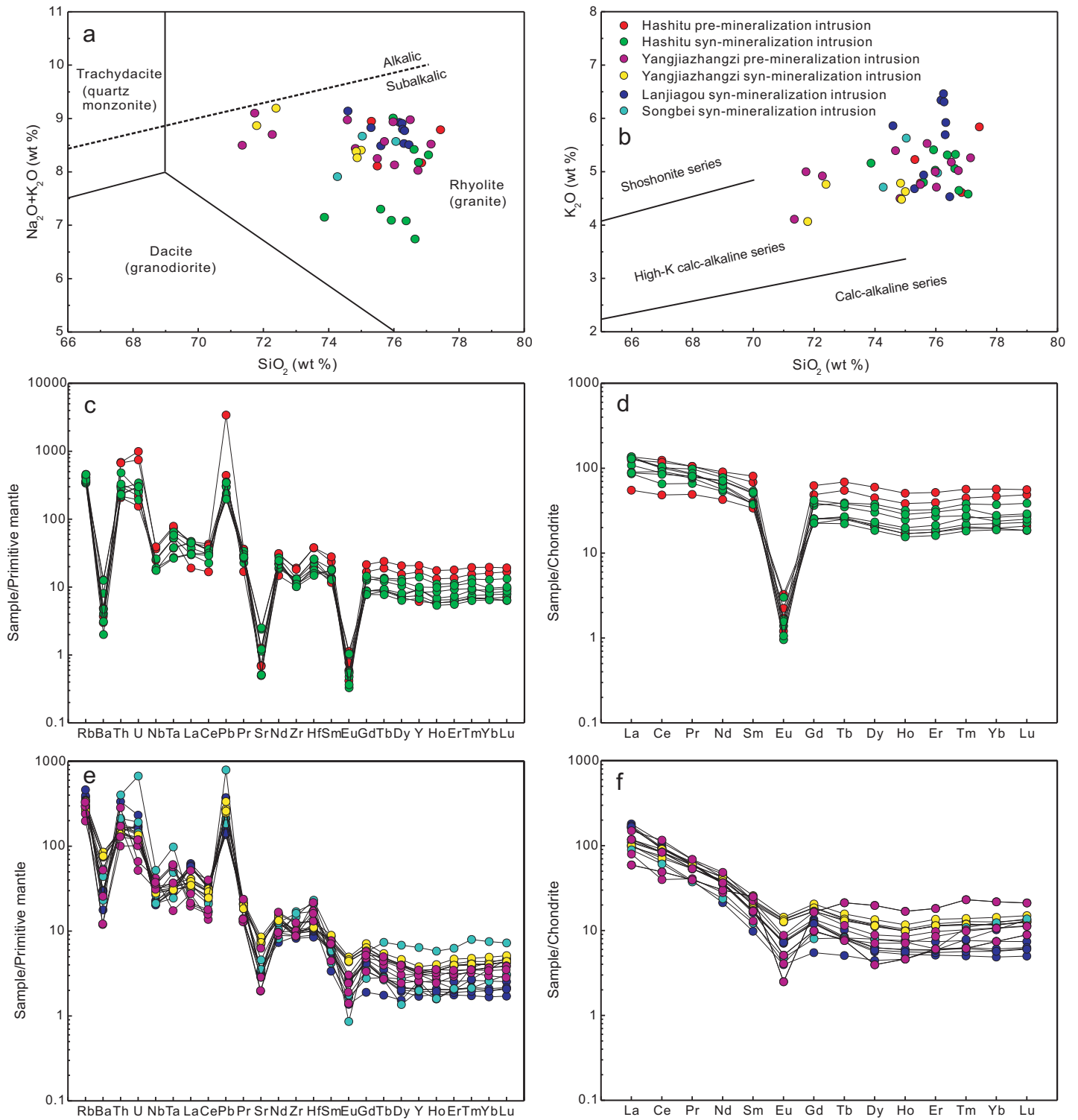


Fig 3

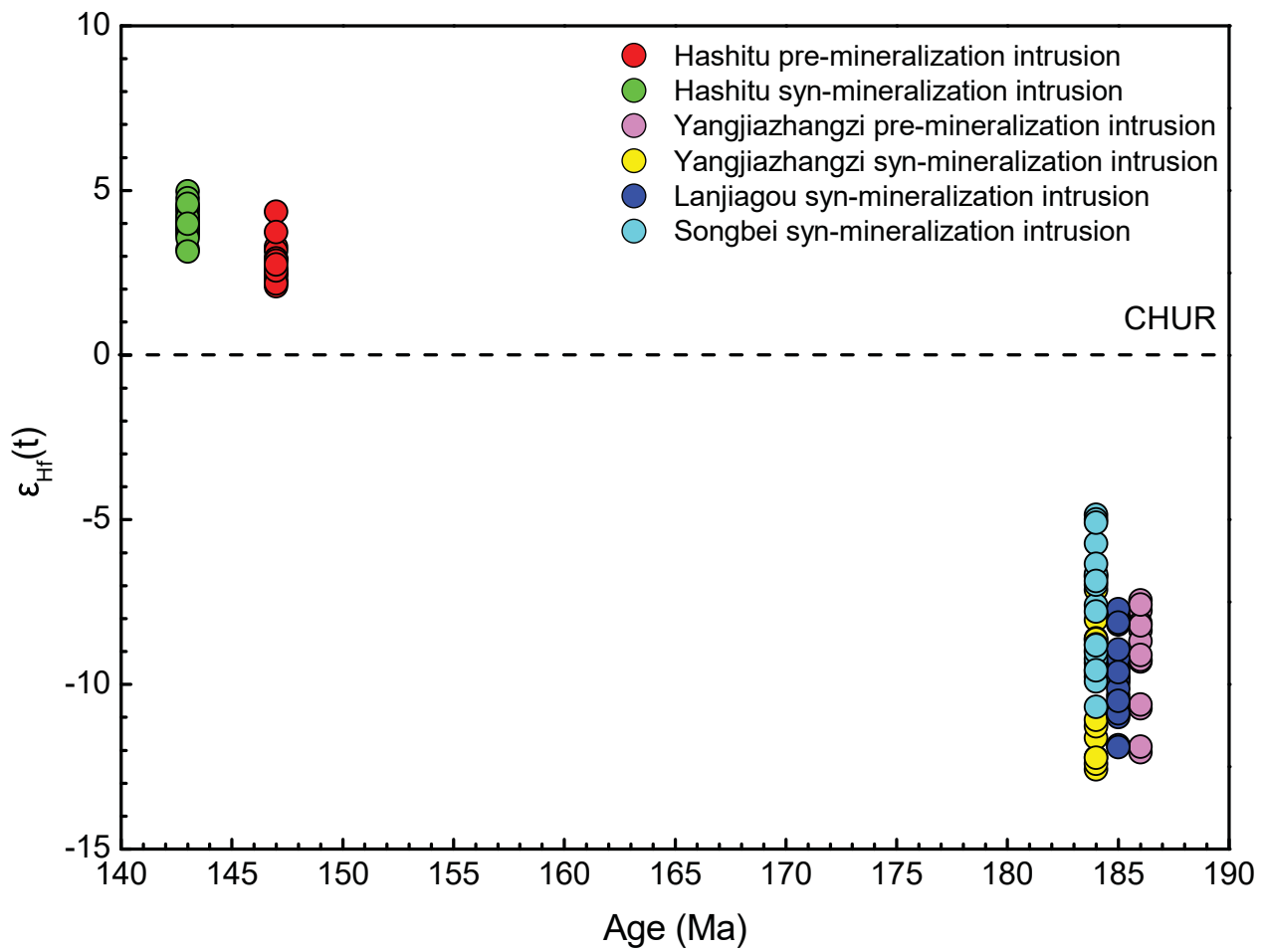


Fig 4

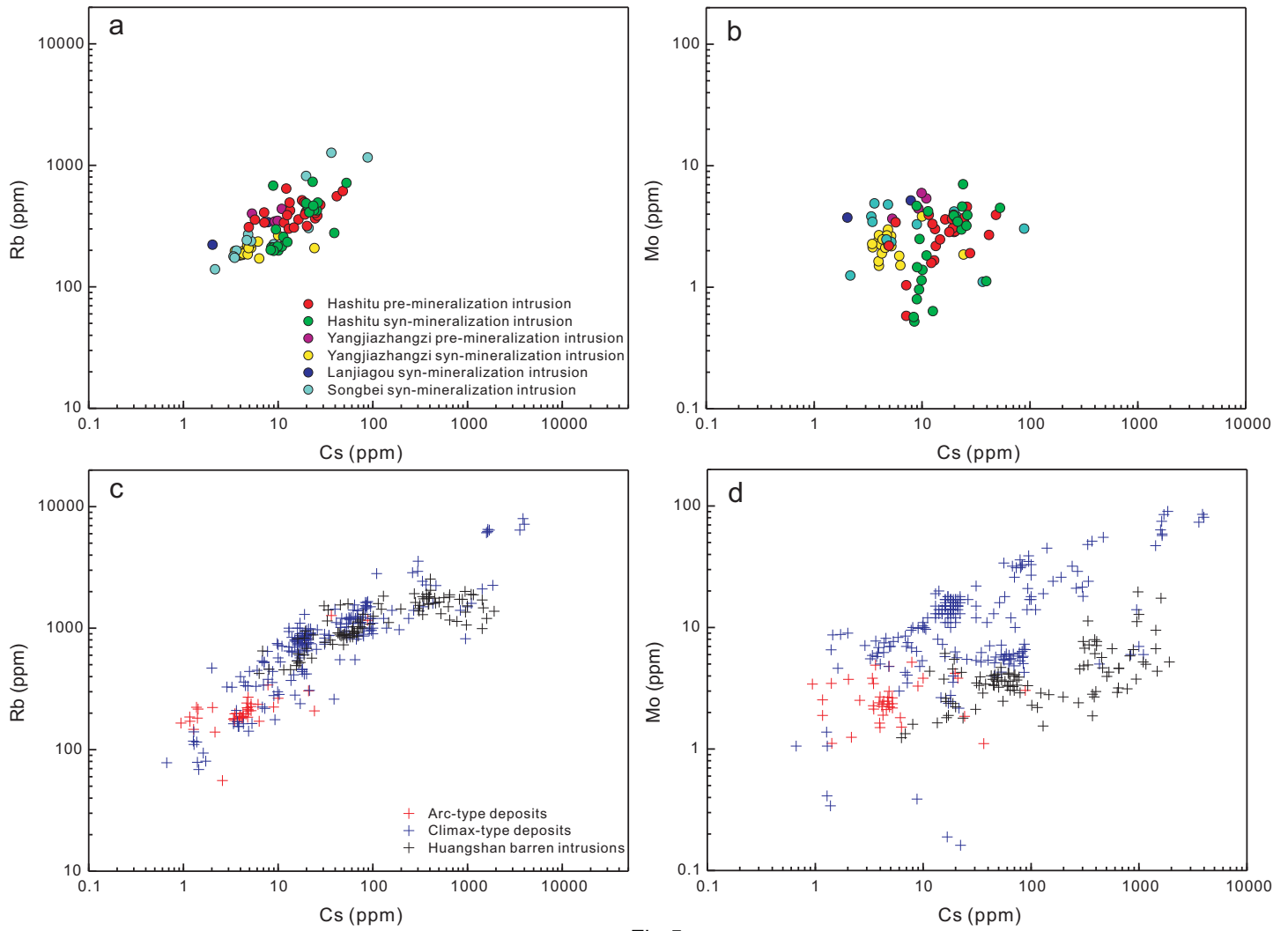
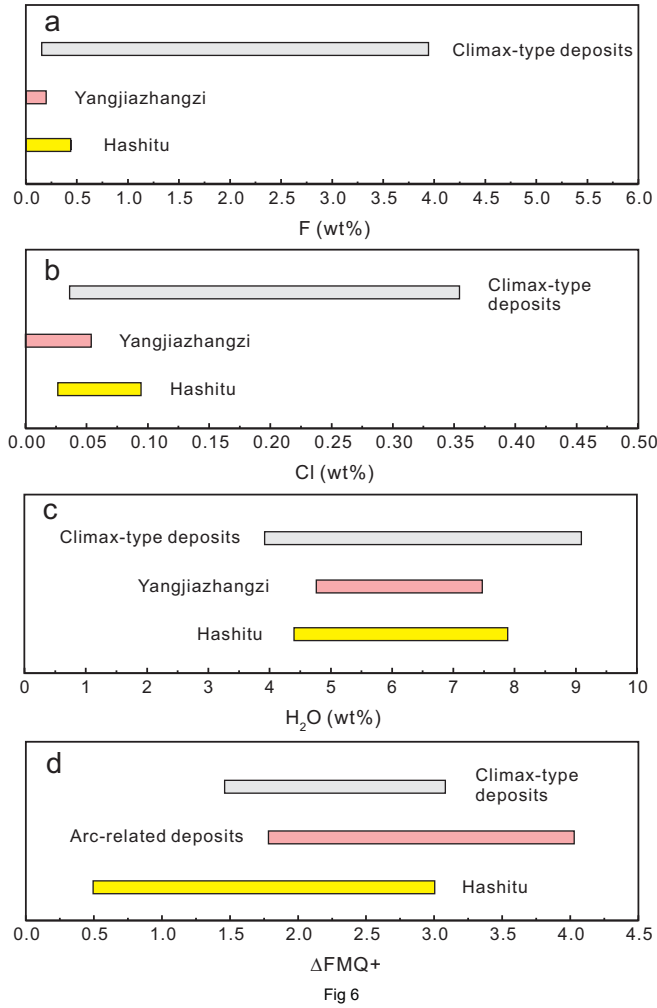


Fig 5



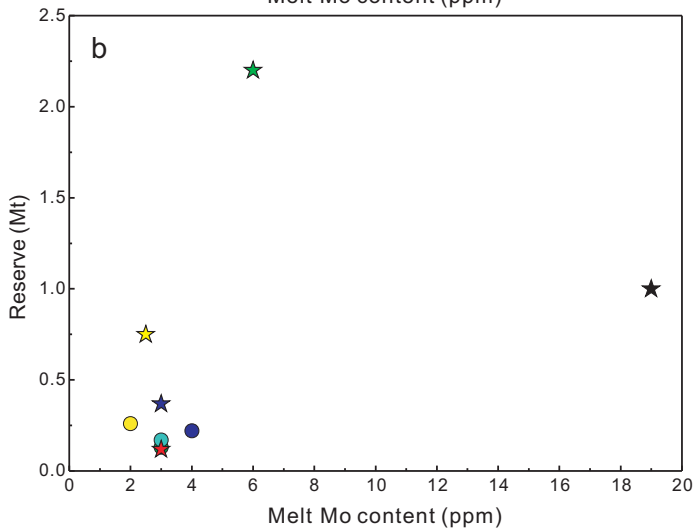
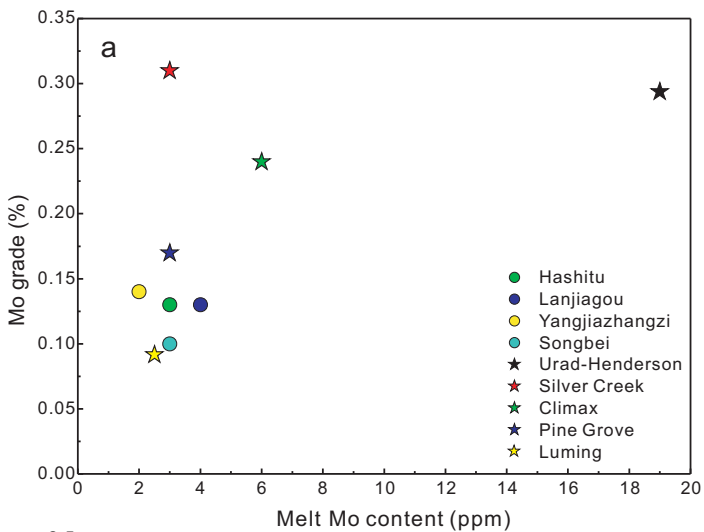


Fig 7

